Effect of viscosity ratio on the self-sustained instabilities in planar immiscible jets

Outi Tammisola,* Jean-Christophe Loiseau, and Luca Brandt
KTH Mechanics, KTH Royal Institute of Technology, Osquars Backe 18, 10044 Stockholm, Sweden
(Received 21 September 2016; published 21 March 2017)

Previous studies have shown that intermediate magnitude of surface tension has a counterintuitive destabilizing effect on two-phase planar jets. In the present study, the transition process in confined two-dimensional jets of two fluids with varying viscosity ratio is investigated using direct numerical simulations (DNSs). The outer fluid coflow velocity is 17% of that of the central jet. Neutral curves for the appearance of persistent oscillations are found by recording the norm of the velocity residuals in DNS for over 1000 nondimensional time units or until the signal has reached a constant level in a logarithmic scale, either a converged steady state or a "statistically steady" oscillatory state. Oscillatory final states are found for all viscosity ratios ranging from 10^{-1} to 10. For uniform viscosity ($m = 1$), the first bifurcation is through a surface-tension-driven global instability. On the other hand, for low viscosity of the outer fluid, there is a mode competition between a steady asymmetric Coanda-type attachment mode and the surface-tension-induced mode. At moderate surface tension, the first bifurcation is through the Coanda-type attachment, which eventually triggers time-dependent convective bursts. At high surface tension, the first bifurcation is through the surface-tension-dominated mode. For high viscosity of the outer fluid, persistent oscillations appear due to a strong convective instability, although it is shown that absolute instability may be possible at even higher viscosity ratios. Finally, we show that the jet is still convectively and absolutely unstable far from the inlet when the shear profile is nearly constant. Comparing this situation to a parallel Couette flow (without inflection points), we show that in both flows, a hidden interfacial mode brought out by surface tension becomes temporally and absolutely unstable in an intermediate Weber and Reynolds regime. By an energy analysis of the Couette flow case, we show that surface tension, although dissipative, can induce a velocity field near the interface that extracts energy from the flow through a viscous mechanism. This study highlights the rich dynamics of immiscible planar uniform-density jets, where different self-sustained and convective mechanisms compete and the nature of the instability depends on the exact parameter values.

DOI: 10.1103/PhysRevFluids.2.033903

I. INTRODUCTION

Two-phase flows are encountered in numerous industrial applications such as oil and gas transport, the atomization of jets in fuel injectors, and even in microfluidics. Over the past decades, the understanding of the initial stage of the transition to turbulence in such two-phase flows has essentially relied on the use of local stability theory. This local approach, based on the parallel flow assumption, allows one to investigate the linear stability of unidirectional base flows toward infinitesimal perturbations having a given streamwise and/or spanwise periodicity. Using this local ansatz, Boomkamp and Miesen [1] proposed a classification of the different linear instability mechanisms existing in interfacial flows based on a careful inspection of the perturbation energy budget. Their review indicated that, in many of the two-phase flow situations investigated until then,

*Also at Faculty of Engineering, The University of Nottingham, University Park, Nottingham NG7 2RD, United Kingdom; outi@mech.kth.se

the dominant instability mechanism results from a viscosity stratification that leads to net work being done by the perturbation velocity and stress at the interface separating the two phases. As for single-phase flows, shear-driven linear instabilities (such as Tollmien-Schlichting waves) are also of importance and can even compete with the viscosity stratification mechanism as was shown by Yecko *et al.* [2] for two-phase mixing layers. On the other hand, viscosity stratification may also invoke other instability mechanisms such as short-wave instability.

One mechanism by which the viscosity stratification causes instability in confined shear flows is the long-wave Yih mechanism [3,4]. The seminal work of Yih found that Couette and Poiseuille flows become unstable for all Reynolds numbers if the outer fluid is more viscous [3]. Later, Hooper and Boyd [5] showed that Couette flow of two fluids in the absence of surface tension is always unstable to short waves. The mechanism for the short-wave instability due to viscosity stratification was analyzed by Hinch [6].

These studies were based on an initially parallel base flow and rely on a local temporal stability approach to explain the initial stage of transition. In such a local temporal framework, surface tension either is often negligible or has a stabilizing effect on the instability (see, e.g., the classification by Boomkamp and Miesen [1]). However, when investigating the local absolute instability properties of a top-hat wake profile, Rees and Juniper [7] observed that surface tension increases the absolute growth rate of the instability in an inviscid model problem.

Absolute instabilities can be related to what is known as global instability modes in nonparallel flows. Investigating the stability of such nonparallel flows (what is now known as global linear stability) has proven helpful in numerous single-phase flow situations to get a better understanding of the underlying physics. Unfortunately, probably because of its computational complexity, such a global approach to linear instability is still scarcely used to investigate strongly nonparallel two-phase flows. Tammisola *et al.* [8,9] used the global approach on two-fluid flows by solving the linearized Navier-Stokes equations numerically in both phases (and not treating either as inviscid, in which case analytical solutions could have been found). In Ref. [9] the global instability of two-phase confined coflowing jets and wakes with constant density and viscosity was investigated. Intermediate values of surface tension were found to cause global instability in jet flows that were robustly globally stable otherwise. For wakes [8,9], intermediate surface tension gives rise to global modes with considerably higher growth rates than the von Kármán mode. In both cases, strong enough surface tension eventually stabilizes the global instability modes. Biancofiore *et al.* [10] provided a physical explanation for the counterintuitive destabilization of wake flows by intermediate surface tension. The system was modeled as a broken-line shear layer, where counterpropagating Rossby waves formed at the vorticity discontinuities and capillary waves at the interface. By considering the resulting wave interaction, they deduced that intermediate surface tension could cause local temporal and absolute instability.

The global linear predictions [8] on the wake flows were partly confirmed by Biancofiore *et al.* [11] using direct numerical simulations (DNSs). While their calculations reveal relatively good agreement regarding the promotion of wake instability at intermediate surface tension, they did not observe at all the varicose instability modes for wakes predicted by global linear instability [9]. A possible explanation given by Biancofiore *et al.* [11] was that the base flows in Ref. [9] were computed in the absence of surface tension. Also, the observed wake instability due to surface tension saturated nonlinearly to such a low amplitude that the interface remained flat. Hence, the large effects on both jets and wakes indicated by linear global analysis still remained to be confirmed in nonlinear simulations. All that the DNS [11] seemed to show was that the surface tension merely altered the von Kármán instability of wakes to another, very weak, instability mode.

Moreover, the above-mentioned studies assumed the same density and viscosity of the two fluids. This assumption hardly holds for a generic two-fluid flow and raises the question of how the density and viscosity ratios might alter the global instability behavior. *A priori*, the influence of the viscosity ratio is hard to predict. The viscosity ratio could act by simply changing the effective Reynolds number of the two-fluid flow, thus changing the critical Reynolds number accordingly. However, there could be an interplay of different instability mechanisms. The study of Tammisola

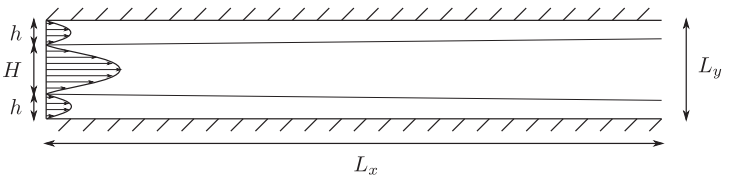

FIG. 1. Illustration of the flow geometry.

et al. [9] identified surface tension and inflow shear as the dominant parameters for the viscosity ratio $m = 1$. However, as shown in numerous local stability analyses, viscosity stratification often drives the local instability properties of parallel flows through either the Yih mechanism [3] or the short-wave instability mechanism [5]. Furthermore, viscosity may affect the instability by changing the spatial development of the two-dimensional base flow, such as the presence of recirculation regions.

The present study is a continuation of previous studies on coflow jets and wakes and has two main aims: (i) to confirm the surprising destabilization of jet flows in nonlinear simulations and (ii) to investigate how the viscosity ratio affects the presence of self-sustained oscillations (global instability). To this end, DNSs are performed using our in-house DNS optimized interfacial level-set (OILS) solver, derived from the two-phase level-set (TPLS) open-source code [12], which was successfully used recently to study the nonlinear development of the Yih instability [13].

II. STATEMENT OF THE PROBLEM

The flow considered is that of two immiscible fluids in a planar channel as depicted in Fig. 1. In this configuration, an inner fluid stream (fluid 1) is symmetrically sandwiched between two outer streams of fluid 2. The geometry and inflow are symmetric with respect to the centerline ($y = 0$). In the following, H denotes the channel height, $\bar{U}_1$ and $\bar{U}_2$ denote the bulk velocity of fluids 1 and 2 at the inflow, μ_1 and μ_2 are their viscosities, and γ is the surface tension between them.

Varying all relevant parameters would result in a huge number of simulations and hence several of them are fixed. The half height of the inner fluid is set equal to $H/2$, which means that the confinement parameter (denoted by h in Refs. [9,14] and not to be confused with the interfacial height h in this work) is 1.0 throughout this work. The fluids have the same uniform density ρ. The shear ratio $\Lambda^{-1} = (\bar{U}_1 + \bar{U}_2)/(\bar{U}_1 - \bar{U}_2)$, with $\bar{U}$ the average inflow velocity of each layer, will be fixed at $\Lambda^{-1} = 1.4$. The flow case considered is thus a coflow jet [9]; the inner flow stream has the highest velocity. The average inflow velocity of the outer fluid is 17% of that of the inner fluid.

The remaining parameters are the Reynolds number $\mathrm{Re} = \rho \bar{U}_1 H/2\mu_1$, the viscosity ratio $m = \mu_2/\mu_1$, and the Weber number $\mathrm{We} = \rho \bar{U}_1^2 H/2\gamma$. Varying all three parameters simultaneously in the DNS would still be very expensive and make the visualization of neutral surfaces in such a large parameter space complicated. Hence, we vary the Reynolds number and viscosity ratio, while the Weber number is fixed at $\mathrm{We} = 10$ in the DNS except in Sec. IV F; it will be varied in the Couette flow model problem. It should be noted that this jet is globally stable for all shear ratios without surface tension when $m = 1$, but becomes globally unstable at moderate Reynolds numbers when $\mathrm{We} = 10$ [9].

III. GOVERNING EQUATIONS AND NUMERICAL METHODS

The dynamics of this flow is governed by the two-fluid incompressible Navier-Stokes equations with jump conditions at the interface between the two fluids. The previous global instability studies [8,9] were performed with a sharp interface approach with two different domains for the two fluids, with coupling conditions at the interface. The present DNS study is performed

by a diffuse-interface approach. During this work we have developed an in-house solver OILS, which is based on the open-source solver TPLS [12], which was successfully validated against local instability studies in Ref. [13]. Both TPLS and OILS use a level-set approach along with a continuous-surface-tension model (see [15]) to model the interface separating the two phases. The viscosity discontinuity and surface-tension force are both smoothed over a region of 1.5 grid cells and are continuous functions around the interface. In such a formalism, the Navier-Stokes equations governing the dynamics of the two-phase flow are given by

$$\begin{aligned} \frac{\partial \phi}{\partial t} + \mathbf{U}\cdot\nabla\phi &= 0, \\ \frac{\partial \mathbf{U}}{\partial t} + (\mathbf{U}\cdot\nabla)\mathbf{U} &= -\nabla P + \frac{1}{\mathrm{Re}}\nabla\cdot[\mu(\nabla\mathbf{U}+\nabla\mathbf{U}^T)] + \frac{1}{\mathrm{We}}\kappa\delta_\epsilon(\phi)\mathbf{n}, \\ \nabla\cdot\mathbf{U} &= 0, \end{aligned} \tag{1}$$

where $\mathbf{U}$ and P are the velocity and pressure fields, respectively. The function $\phi(\mathbf{x},t)$ is the level-set function, indicating which fluid occupies the point $\mathbf{x}$ at a given instant of time t ($\phi < 0$ for fluid 1 and $\phi > 0$ for fluid 2). Consequently, the height of the interface $h(\mathbf{x},t)$ separating the two fluids is given by the zero level-set contour: $\phi(\mathbf{x},t) = 0$. The level-set function is used to determine the unit vector $\mathbf{n}$ normal to the interface and the local curvature κ:

$$\begin{aligned} \mathbf{n} &= \frac{\nabla\phi}{\|\nabla\phi\|}, \\ \kappa &= -\nabla\cdot\mathbf{n}. \end{aligned} \tag{2}$$

The viscosity jump is expressed as

$$\mu = m[1 - H_\epsilon(\phi)] + H_\epsilon(\phi),$$

where $H_\epsilon(\phi)$ is a regularized Heaviside function smoothed across a width $\epsilon = 1.5\Delta x$. Similarly, the function $\delta_\epsilon(\phi)$ in Eq. (1) is a regularized Dirac function with a compact spatial support on the interval $[-\epsilon,\epsilon]$.

A. Computational domain and boundary conditions

The computational domain (shown in Fig. 1) has the dimensions $[0,L_x]\times[-L_y/2,L_y/2]$. In this study, $L_y = 4$ is given by the nondimensionalization. In the x direction, the length was chosen to be $L_x = 250$. This length was found to be sufficient for surface-tension-driven linear global modes in Ref. [9], which was also confirmed by our initial DNS.

Several boundary conditions are needed in order to close the system of equations (1). For the velocity, no-slip boundary conditions are imposed on both the upper and lower walls of the channel, while a standard outflow boundary condition (i.e., $\partial_x\mathbf{U} = p = 0$) is prescribed at the outlet. The inlet velocity profile results from three Poiseuille streams joining at the inflow such that

$$U(y) = \begin{cases} \frac{3}{2}\frac{(\Lambda^{-1}-1)}{(\Lambda^{-1}+1)}[1-4(y-1.5)^2] & \text{for } y > 1 \\ \frac{3}{2}(1-y^2) & \text{for } -1 \leqslant y \leqslant 1 \\ \frac{3}{2}\frac{(\Lambda^{-1}-1)}{(\Lambda^{-1}+1)}[1-4(y+1.5)^2] & \text{for } y < -1, \end{cases}$$

where $\Lambda = 1.4$ is the shear ratio defined previously. Regarding the level-set function ϕ, a Neumann boundary condition is imposed at the outlet, while at the inlet

$$\phi(y) = \begin{cases} 1+z & \text{for } z < 0 \\ 1-z & \text{for } z \geqslant 0. \end{cases}$$

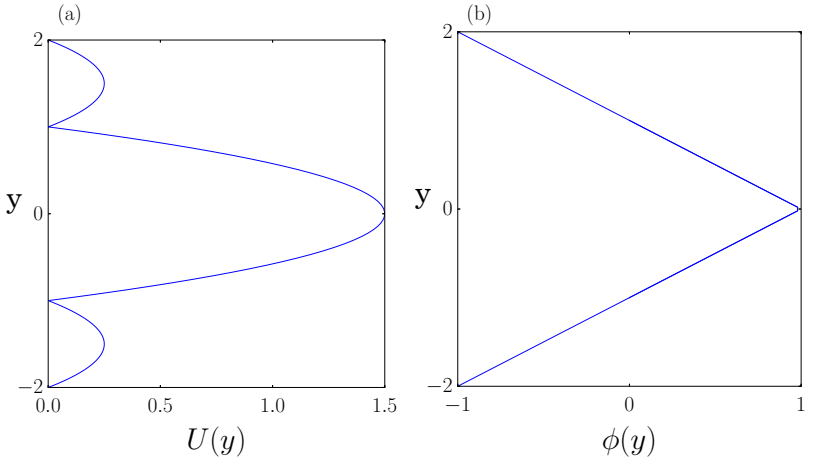

FIG. 2. Illustration of the inflow profiles: (a) inflow velocity profile for $\Lambda^{-1} = 1.4$ and (b) inflow level-set profile.

For the sake of illustration, Fig. 2 depicts the inlet velocity profile for $\Lambda^{-1} = 1.4$ along with the inlet level-set profile.

B. Discretization scheme

The solver OILS uses the same finite-difference discretization as TPLS [13]. The Navier-Stokes equations are discretized using a finite-volume method on a marker-and-cell grid with uniform grid spacing in all directions of space. The velocities are defined on the cell faces, while the scalars (level-set function ϕ, pressure P, and viscosity μ) are defined at the cell centers. A fully explicit second-order Adam-Basforth scheme is used for the temporal discretization of the Navier-Stokes equation and a strong-stability-preserving Runge-Kutta 3 scheme (SSPRK3) for the discretization of the level-set advection equation. The pressure and associated divergence-free constraint are treated using the projection method. A Poisson solver based on the scheduled relaxation Jacobi method [16] has been used for the two-dimensional simulations in the present work, while the latest version of OILS instead contains a conjugated gradient solver preconditioned by the algebraic multigrid method. Finally, the level-set function $\phi(\mathbf{x},t)$ is the signed-distance function such that $\|\nabla\phi\| = 1$ and is advected using the high-order upstream-central scheme to fifth-order accuracy (HOUC5) [17]. The redistancing of the resulting level-set function is performed using the partial differential equation–based approach and the algorithm of Sussman and Fatemi [15]. As for the advection of the level-set field, the pseudotime discretization is based on the SSPRK3 scheme, while the spatial discretization now relies on a weighted essentially nonoscillatory scheme accurate to fifth order (WENO5).

Regarding resolution, in initial studies, 128 points in the wall-normal direction (resulting in a grid spacing of $\delta x = \delta y = 7.8 \times 10^{-3}$) were found to be sufficient for most parameter values and are used throughout this work, except for the lowest viscosity ratio ($m = 0.1$), for which 256 points in the wall-normal direction ($\delta x = \delta y = 3.9 \times 10^{-3}$) were needed to fully capture the details of the interfacial waves and the wall boundary layer.

IV. RESULTS

A. Presence of a global instability in DNS for uniform viscosity coflow jets ($m = 1$)

The first study to be performed is to confirm that the surface-tension-induced instability of coflow jets [9] found by linear global mode analysis also appears in nonlinear simulations (DNSs). If very

close to a neutral stability boundary, the flow in the DNS first turns towards the base flow, which is a steady solution to the Navier-Stokes equations (here expressed in the level-set formalism)

$$\begin{aligned}\mathbf{U}_b \cdot \nabla \phi_b &= 0,\\ (\mathbf{U}_b \cdot \nabla)\mathbf{U}_b &= -\nabla P_b + \frac{1}{\mathrm{Re}}\nabla \cdot \left[\mu\left(\nabla \mathbf{U}_b + \nabla \mathbf{U}_b^T\right)\right] + \frac{1}{\mathrm{We}}\kappa \delta_\epsilon(\phi)_b \mathbf{n},\\ \nabla \cdot \mathbf{U}_b &= 0.\end{aligned} \tag{3}$$

Close to the neutral global stability limit and if convective instabilities are not too strong, the appearance of global instability can be quantified in DNS by looking at time traces of the velocity.

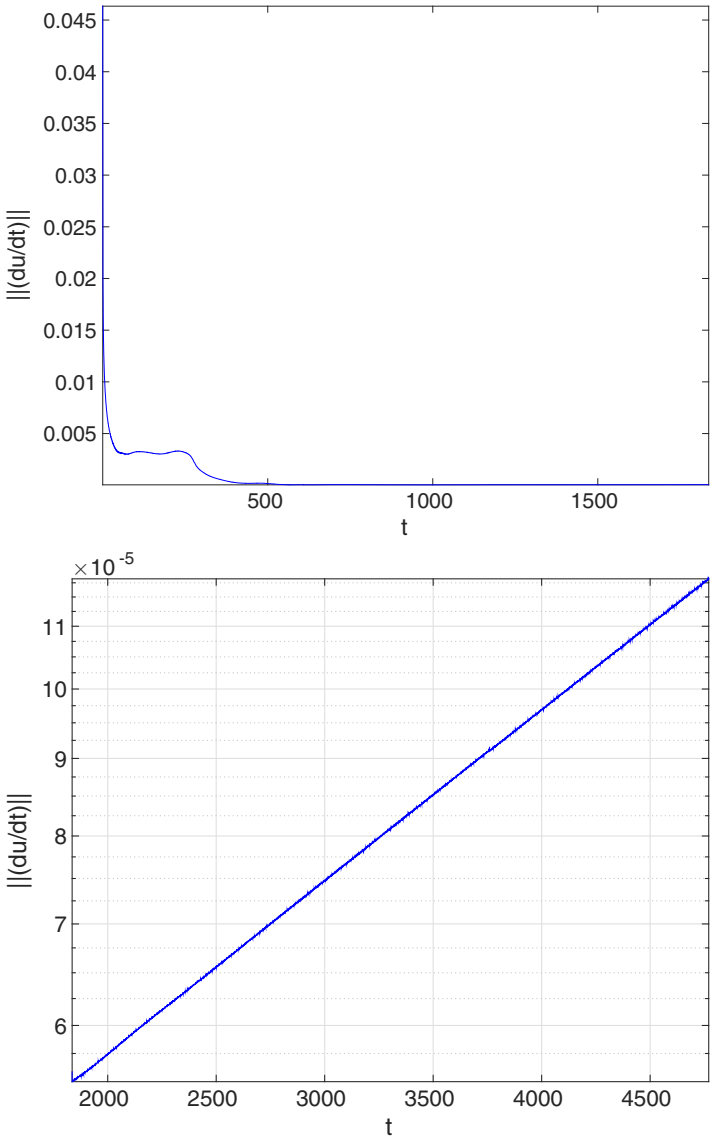

FIG. 3. Shown on top is the norm of the average time derivative over the flow domain over time, at $m = 1$ and $\mathrm{Re} = 250$. This shows the initial decay towards steady state. The bottom is the same but at later times and in logarithmic (y) scale. This shows the initial exponential growth of a linear global mode, which will saturate to a constant-amplitude limit cycle at later times.

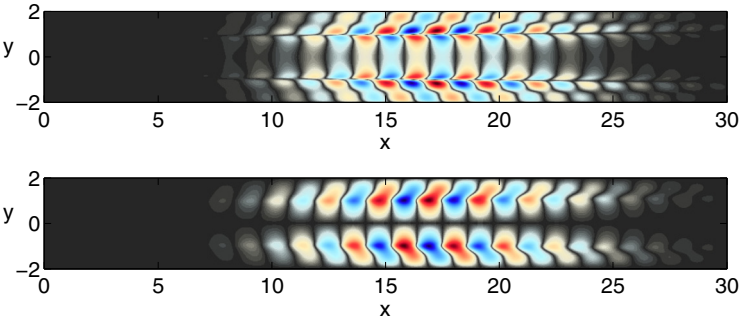

FIG. 4. Difference between the instantaneous velocity from DNS and the steady solution, at $m = 1$ and $\mathrm{Re} = 250$, during the exponential growth phase for the streamwise velocity field (top) and the vertical velocity field (bottom).

When an unstable global mode is present, the DNS time signal in any given point in space grows exponentially in time. If the global modes are all stable ($\sigma_r < 0$ for all modes), then the time trace should exhibit an exponential decay.

In this study, time-dependent oscillations are quantified by recording the spatial average of the time derivative of the velocity magnitude over the whole computational domain, simply termed the residual in the rest of this study, given by

$$(L_x L_y)^{-1} \int_D \|\mathbf{u}(t+\delta t) - \mathbf{u}(t)\|/\delta t, \tag{4}$$

where $\int_D$ denotes an integration over the whole computational domain. This residual is shown for $m = 1$ and $\mathrm{Re} = 250$ in Fig. 3. It shows a clear initial decay towards a steady state U_b (top) and a later exponential growth in the vicinity of the steady state (bottom). Such observation indicates that a linear global mode is growing in the DNS and the flow at $\mathrm{Re} = 250$ is hence globally unstable. A similar study for $\mathrm{Re} = 245$ shows an exponentially decaying residual, indicating that the flow in DNS is stable. A linear interpolation between the two growth and decay rates gives a neutral point and the critical Reynolds number $\mathrm{Re}_c = 248$.

The growing eigenmode is depicted in Fig. 4. The oscillation displays short-wavelength waves localized around the interface, in the upstream part of the computational domain. The unstable global eigenmodes for the jet in Fig. 6 of Ref. [9] (at $\Lambda^{-1} = 1.2$ and $\mathrm{Re} = 316$) also had short-wavelength waves around the interface at a similar wavelength. Knowing that both jets are globally stable without surface tension (observed in the present work as well as in Ref. [9]), the resemblance strongly indicates that we are observing the same surface-tension-induced global instability. It is also worth investigating whether the jet modes saturate at a very low level and without visible interface perturbation, as was indicated especially for the varicose wake mode in Ref. [11]. First, Fig. 5 shows the vertical velocity $V(x,y)$ of the final oscillatory state at $m = 1$ (without subtracting

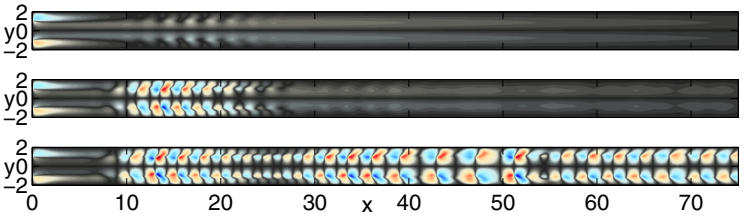

FIG. 5. Vertical velocity field at the saturated nonlinear state at $m = 1$ and $\mathrm{Re} = 250$ (top), $\mathrm{Re} = 316$ (middle), and $\mathrm{Re} = 500$ (bottom). The color scale limits are ± 0.1 in all figures.

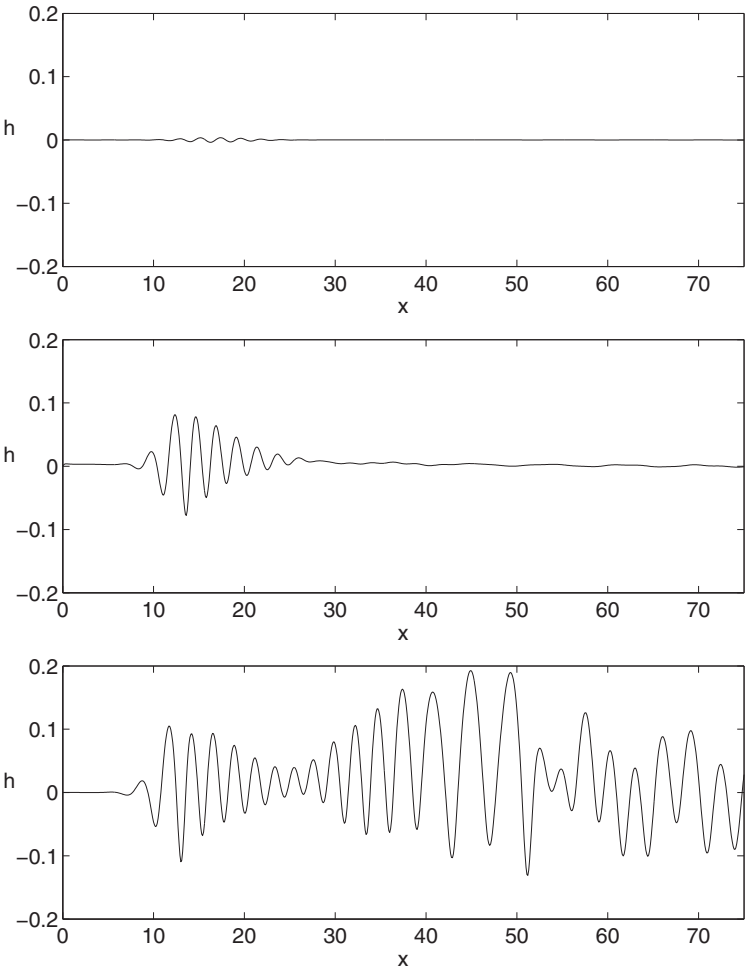

FIG. 6. Instantaneous (upper) interface position, mean value subtracted, at the saturated nonlinear state at $m = 1$ and $\mathrm{Re} = 250$ (top), $\mathrm{Re} = 316$ (middle), and $\mathrm{Re} = 500$ (bottom).

the base flow), at increasing Reynolds numbers, from $\mathrm{Re} = 250$ at the top to $\mathrm{Re} = 500$ at the bottom. When the Reynolds number increases, the amplitude of the vertical velocity oscillation increases significantly and the mode becomes much more elongated in the streamwise direction. The interfacial perturbation amplitudes at different Reynolds numbers can be compared in Fig. 6. At bifurcation ($\mathrm{Re} = 250$, top), the maximal interface displacement is $|h| = 0.004$, which is barely visible and is comparable to the wake modes in Ref. [11] at $|h| = 0.01$. At $\mathrm{Re} = 500$, the global instability perturbs the interface significantly, up to $|h| = 0.19$.

B. Local stability analysis

It is instructive to find out where the absolute instability driving the global mode is located. A local spatiotemporal analysis has been performed for the jet flow slightly above the onset of instability: $m = 1$ and $\mathrm{Re} = 250$. Exactly one absolutely unstable mode was found: This is a hidden neutral mode destabilized by surface tension, called the interfacial mode in Refs. [8,9]. The mode is symmetric (varicose), in agreement with the DNS shown in the preceding section.

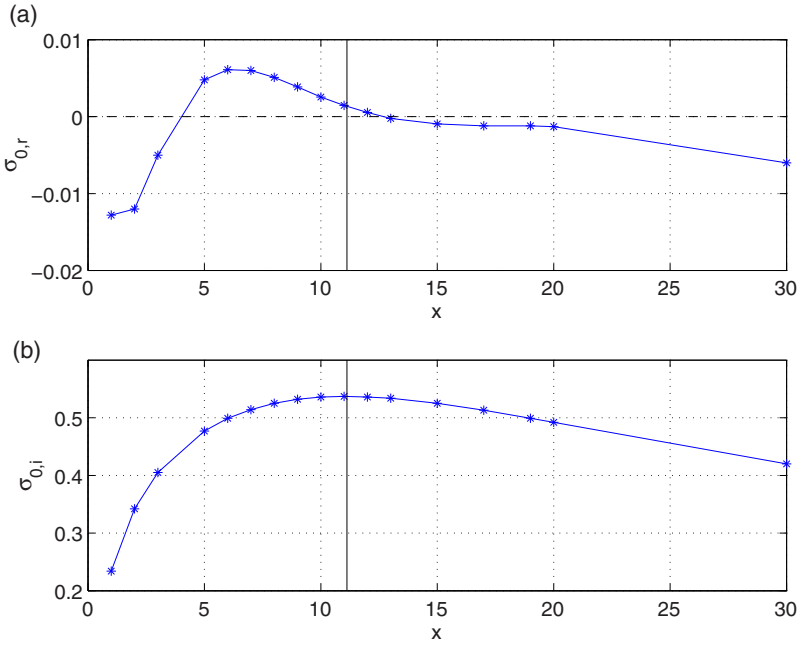

FIG. 7. Local absolute frequency of the base flow computed by TPLS at $m = 1$ and $\mathrm{Re} = 250$: (a) absolute growth rate $\sigma_{0,r}$ and (b) absolute frequency $\sigma_{0,i}$. The vertical line indicates the position of the saddle in the complex X plane.

The streamwise evolution of the local absolute growth rate is shown in Fig. 7(a), while that of the local absolute frequency is presented in Fig. 7(b). The flow displays a pocket of absolute instability between $x = 4$ and $x = 13$. The maximum absolute growth $\sigma_{r,\max} = 0.06$ occurs at $x = 6$. The approximate global mode frequency and wave-maker position can be found by an analytic continuation of σ_0 to the complex X plane. This is done here by fitting Padé polynomials around the point of maximum absolute growth, as in Ref. [18]. The linear global mode frequency approximated by local spatiotemporal analysis this way is $\sigma_{g,l} = 0.0013 + 0.54i$. The angular frequency extracted from the DNS time signal during the exponential growth is 0.53, in very good agreement with the local analysis.

The nonlinear oscillation waves observed in Fig. 5 all have a similar envelope upstream in the domain. Further downstream, the modes at $\mathrm{Re} = 250$ and $\mathrm{Re} = 316$ (Fig. 5, top) decay and have negligible amplitudes for $x > 30$. The mode at $\mathrm{Re} = 500$ (Fig. 6, bottom), on the other hand, grows again at $x \approx 30$ and remains at a large amplitude at $x = 75$. In Ref. [9], similar, very elongated jet modes were obtained for a range of parameter values for which a coupling was occurring between the upstream absolute instability pocket and a convective instability pocket downstream (the convective instability having coincidentally the same frequency as the absolute instability). It therefore deserves to be investigated whether the second growth region is due to an absolute or convective instability.[1] Figure 8 shows the absolute instability at $\mathrm{Re} = 500$. This reveals an upstream onset of absolute instability similar to that at $\mathrm{Re} = 250$, at the same frequency ($\sigma_{g,l} = 0.016 + 0.54i$), but the absolute growth at $\mathrm{Re} = 500$ does not decay. The flow instead exhibits an extremely long pocket of absolute instability, until $x \approx 75$. Hence, the long mode observed for $\mathrm{Re} = 500$ is

[1]It should be noted that one should expect only an indicative relation between the nonlinear oscillation shape and absolute instability regions this far from bifurcation.

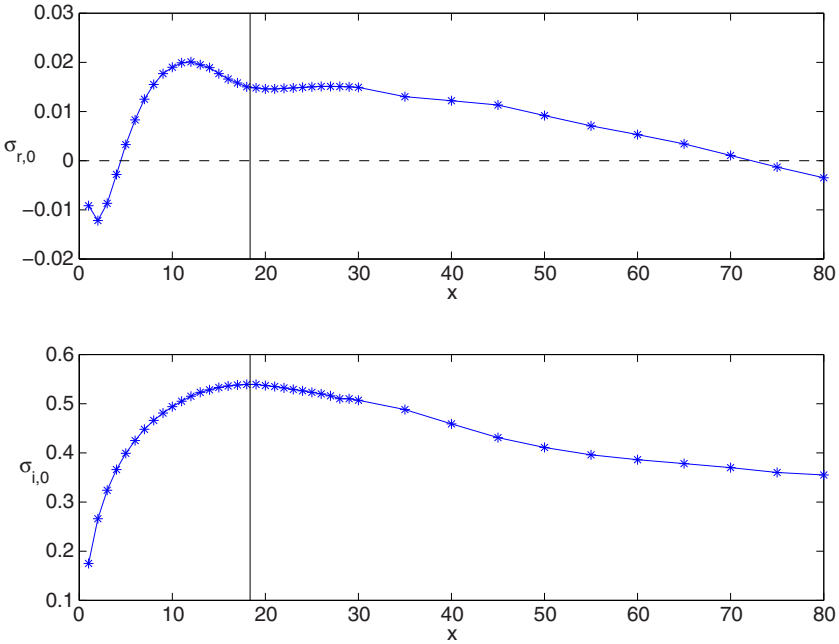

FIG. 8. Same as in Fig. 7 but at $m = 1$ and $\mathrm{Re} = 500$.

due to a persistent absolute instability, in contrast to the elongated modes in Ref. [9] that arose through a coupling of an absolute instability pocket with a second convective instability mode. Long modes of high amplitude can thus arise due to several different mechanisms, further highlighting the rich dynamics exhibited by such a basic flow case as immiscible planar jets with surface tension.

C. Effect of the viscosity ratio on instability

The influence of the viscosity ratio on the instability and transition to unsteadiness is now investigated. We note that for nonuniform viscosity, we could not always observe a clear exponential growth in our time signals. Strong convective instability bursts could be masking a slow exponential growth in time, especially far away from instability boundaries (unknown *a priori*). Hence, our classification of stable or steady and oscillatory flow cases is based on the final saturated flow state. To obtain the neutral curve in the Re-m plane, we have applied the following procedure. First, at each viscosity ratio, we scan a range of Reynolds numbers in the DNS to approximately locate the neutral curve. Closer to the neutral curve, a steady solution for the Navier-Stokes equation (base flow) is obtained using selective frequency damping [19]. Then a new DNS is started from the base flow and the residual and perturbation norm is recorded over a period of at least 1000 (but typically greater than 3000) nondimensional time units. At this point, transients have usually decayed and the state of the flow is "statistically steady," i.e., the average residual over 100 consecutive time units is constant. It should be mentioned that the residual is a time derivative and hence may be higher than the actual perturbation amplitude if high-frequency numerical noise is present. In this work, the following threshold has been adopted: If the final residual and the perturbation amplitude both have settled at a level larger than 10^{-5}, then the flow is classified as unsteady; otherwise, the flow is classified as steady. A table of all simulation times, parameters, and final residual levels is included in Appendix B.

Fifteen different values of the viscosity ratio have been considered, ranging from $m = 0.1$ (the outer fluid is much less viscous than the inner fluid) to $m = 10$ (the outer fluid is much more viscous

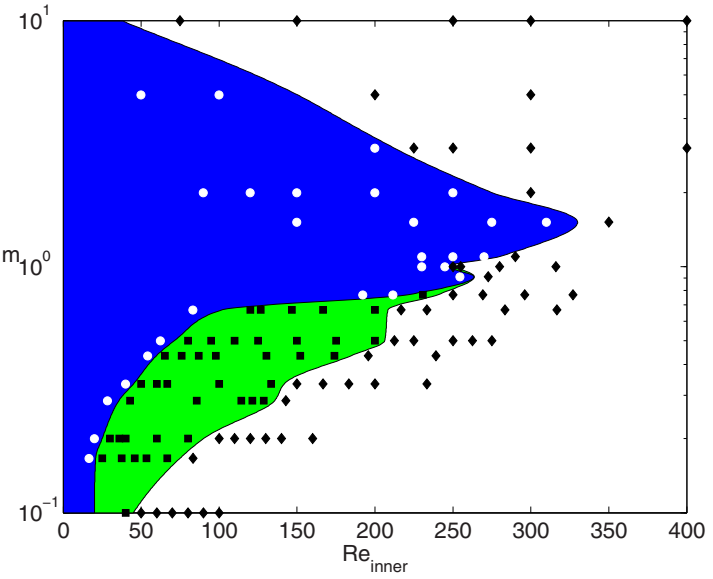

FIG. 9. Neutral stability limit for persistent instability in DNS as a function of the inner flow Reynolds number. In the blue region the flow is stable, in the green region the flow displays a steady Coanda attachment, and in the white region the flow displays time-dependent oscillations. The markers show all the DNS runs, with black markers (on white) denoting persistent oscillation and white markers (on gray) denoting decay of the oscillations (residual settled at a level below 10^{-5}).

than the inner fluid). Regions of steady and oscillatory solutions in the Re-m plane are shown in Fig. 9 as a function of the inner flow Reynolds number. Inside the blue region, the final flow state is stable (steady and symmetric). Inside the white region, the final flow state is unsteady. Inside the green region, the final flow state is steady but asymmetric. The different sets of parameters considered are all depicted by markers.

Figure 9 shows that a small viscosity contrast in any direction (the outer fluid is more viscous or less viscous) is stabilizing. This indicates that the surface-tension-induced global instability is stabilized by a viscosity contrast in any direction. However, the figure clearly highlights that the critical Reynolds number decreases with the viscosity ratio. This indicates that other instability mechanisms are active. The highest critical Reynolds number (the most stable case) $\mathrm{Re}_c \approx 330$ is achieved for a viscosity ratio $m = 1.5$, i.e., when the outer fluid is slightly more viscous than the inner.

Finally, the same trends are observed when the Reynolds number is based on the average viscosity $(\mu_1 + \mu_2)/2$, shown in Fig. 10. It is worth noting moreover that the effective Reynolds number at the onset of instability is not constant for different m. Hence, not only does the viscosity ratio change the effective critical Reynolds number, but it also strongly influences the dominant instability mechanisms.

In the following, the instability mechanisms with more viscous outer fluid ($m > 1$) and less viscous outer fluid ($m < 1$) are analyzed separately. To examine the nature of the instabilities, absolute or convective, we instead rely on space-time diagrams, similarly to [20], where such figures were used to find global instabilities for confined wakes in DNS. The space-time diagram for the supercritical global instability at $m = 1$ and $\mathrm{Re} = 250$ is shown in Fig. 11. The quantity depicted is the sum of the local kinetic energies along the lines $y = 1$ and $y = -1$. The region of the global mode (and absolute instability) is distinctive as a vertical line. The lines of constant amplitude are all vertical, showing that when time increases, the amplitude stays constant in space.

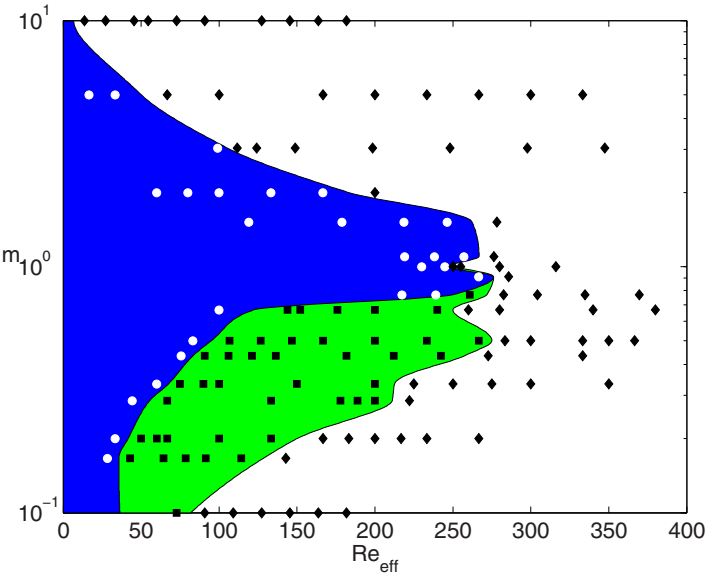

FIG. 10. Same neutral curves and data as in Fig. 9, but shown as a function of the Reynolds number based on average viscosity.

D. Low viscosity of the outer fluid

At $m = 0.9$–1.1, when the Reynolds number is increased from zero, the first bifurcation is through the surface-tension-induced global mode at $\mathrm{Re} \approx 250$. At low enough viscosity of the outer fluid however (approximately $m < 0.9$), a different scenario emerges, which is described below.

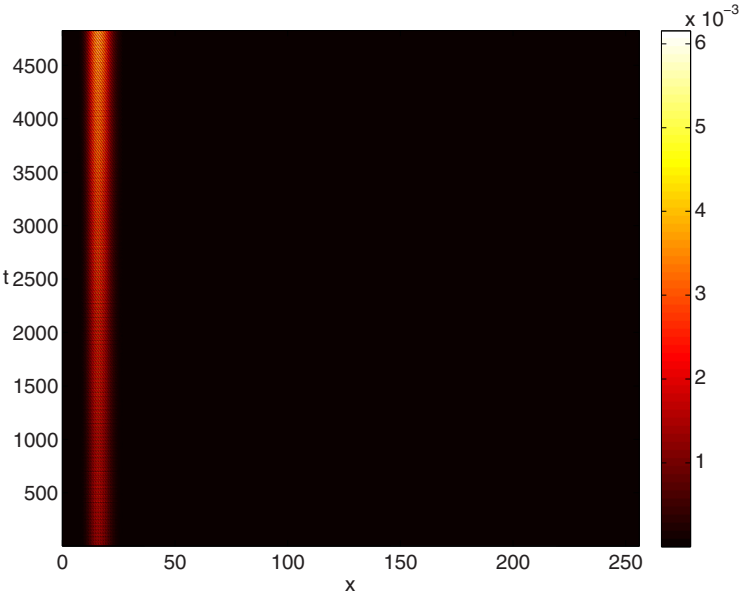

FIG. 11. Space-time diagram of the kinetic energy of the antisymmetric perturbation along the lines $y = \pm 1$, at $m = 1$ and $\mathrm{Re} = 250$. The perturbation grows at the location of the source, which is a sign of global (absolute) instability.

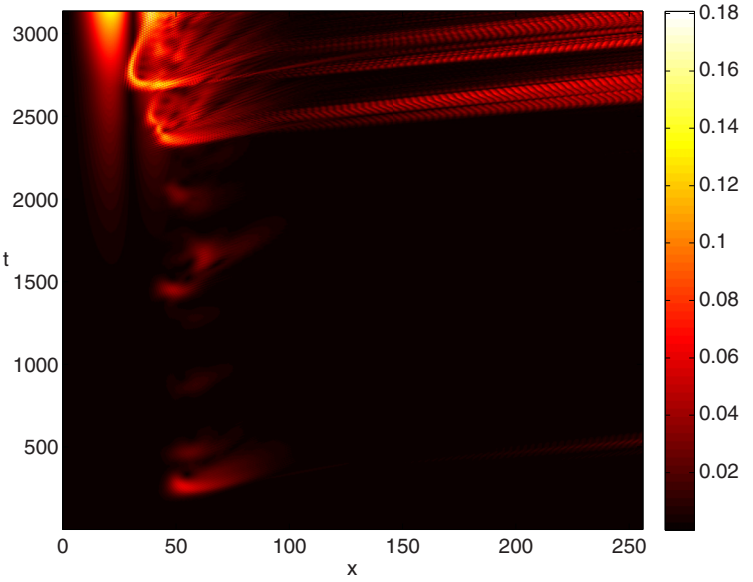

FIG. 12. Space-time diagram of the kinetic energy of the antisymmetric perturbation along the lines $y = \pm 1$, at $m = 0.5$ and $\mathrm{Re} = 250$. This reveals an upstream region of global instability followed by (and triggering) convective bursts downstream.

A space-time diagram for an oscillatory state at $\mathrm{Re} = 250$ (inside the white region) at $m = 0.5$ is shown in Fig. 12. Two regions where the instability grows at the source, around $x = 20$ and $x = 40$, can be observed as two vertical bars. This indicates that a global instability is present. The latter of those regions moreover seems to trigger strong convective instability bursts, i.e., inclined lines that represent wave packets traveling downstream through the domain with a front speed close to 1. The nature of the growing global instability is revealed by looking at the streamwise velocity field at $t = 3100$ (corresponding to the uppermost part of the space-time diagram) in Fig. 13, especially its antisymmetric component (bottom). This is a typical stationary Coanda-type global instability mode, which does not oscillate in time but simply deflects the jet from a symmetric position in the middle towards one of the walls. The symmetric jet has two recirculation bubbles placed symmetrically along each wall. As a result of the Coanda instability, one bubbles has grown in size and the one at the opposite wall has shrunk. The result is a new asymmetric steady state.

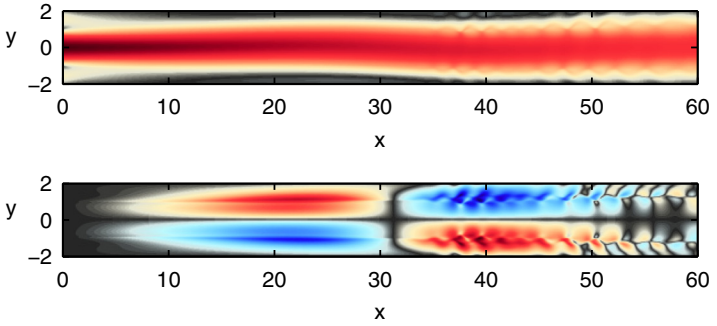

FIG. 13. Streamwise velocity of the flow at $m = 0.5$ and $\mathrm{Re} = 250$ at $t = 3100$ (the uppermost part of the space-time diagram in Fig. 12) for the horizontal velocity field (top) and the antisymmetric part of the same (bottom). Note that the y axis is magnified by a factor 2.5 compared to the x axis.

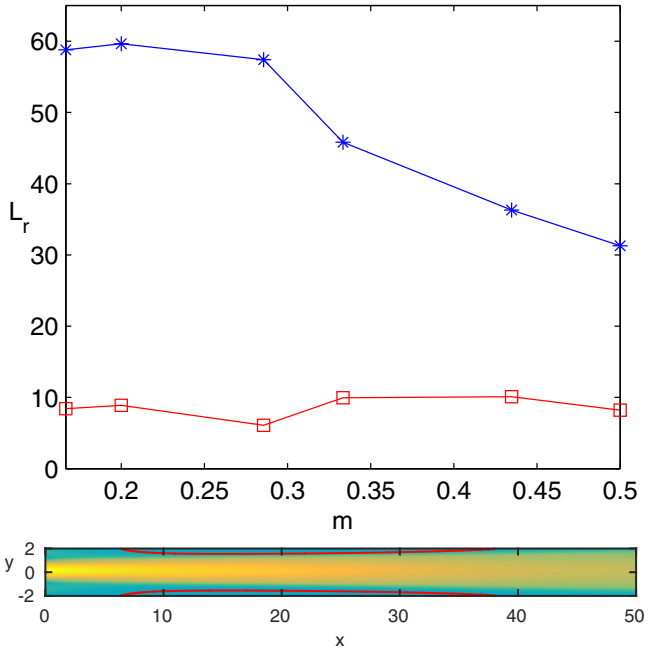

FIG. 14. Shown on top is the recirculation length at constant Re = 230 as a function of m (blue line with stars) and at the onset of Coanda attachment (red line with squares). On the bottom is the streamwise velocity at an early time (before the onset of oscillations or asymmetry). Zero streamwise velocity contour shown in red to emphasize the extent of the recirculation zones.

However, the larger bubble may also trigger convective instability bursts; recirculation bubbles are known to exhibit strong convective instabilities [21]. Similar bursts, or intermittency, developed around a Coanda-type asymmetric flow in a stenosis [22].

By examining the green region in Fig. 9, it appears that the Coanda instability occurs only for $m < 0.9$, i.e., when the outer fluid is less viscous than the inner one. This is because the symmetric base flows with lower outer fluid viscosity contain long regions of reverse flow. In Ref. [23], a critical length of base flow recirculation zones ($L_r \approx 6$) was found at the onset of Coanda instability in a cross junction, for several different parameters. For our jets at Re = 230, the flow with uniform viscosity contains practically no reverse flow (it has a minimum streamwise velocity $U = -10^{-4}$) and neither does the flow with higher viscosity outside. The length of the recirculation zones as a function of m at Re = 230 is shown in Fig. 14, top, blue line, which shows that the recirculation zones severely lengthen towards lower m (up to $L_r = 60$). The red line shows the critical recirculation length at the onset of the Coanda instability for these jets, which stays relatively constant for $L_r = 6$–10.[2] The lengthening of the recirculation zone explains why the flow becomes more unstable at higher viscosity contrasts at the lower end (Fig. 9). A visual demonstration of the separated flow is provided in Fig. 14, bottom, showing the streamwise velocity and its zero contour at $m = 0.2$.

For $m < 0.9$, the first bifurcation always happens through a stationary Coanda mode. For $0.7 < m < 0.9$, the Coanda instability is supercritical. For $m < 0.7$, the Coanda instability is subcritical since a hysteresis is observed: At a fixed Re and m, when starting from a symmetric base flow as an initial condition the final state is symmetric, but when starting from an asymmetric solution at

[2]The critical recirculation length varies more than in Ref. [23] probably because the instability in the present work is subcritical in some regions and supercritical in others.

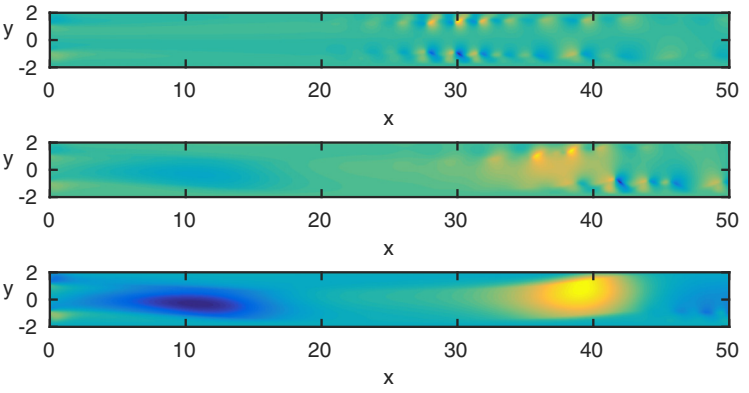

FIG. 15. Instantaneous vertical velocity DNS at $m = 5$ and $\mathrm{Re} = 500$, with time increasing from top to bottom. The jet shows initially short-wavelength waves similar to the uniform density jet, but finally arrives at a steady Coanda attachment.

higher Reynolds number as an initial condition, the final state is asymmetric. The boundary between blue and green regions denotes the subcritical instability boundary; on the left side (stable flow), the final flow state is symmetric irrespective of the initial condition. In Ref. [22], it was observed that a larger hysteresis region can be obtained when making analytic continuations with respect to parameters other than the Reynolds number. If this was done, the boundary may be pushed further to the left. However, in this study we focus on the nature of the instability at different viscosities and therefore further parameter studies have been omitted. Results from all simulations are listed in the tables in Appendix B, where the hysteresis ranges can be found.

At Reynolds numbers above the first bifurcation, a possible mode competition between oscillatory and stationary global modes can be observed before arriving at the stationary asymmetric flow. This is indicated in Fig. 15 at $m = 0.2$ and $\mathrm{Re} = 80$, where time increases from top to bottom. The instability starts in the form of high-frequency small-wavelength waves when the flow state is still nearly symmetric (top), but when the asymmetry develops (middle) these waves are slowly suppressed, until the flow arrives at a nearly steady state (bottom). This flow case belongs to the green region in Fig. 9, where the final state is a steady and asymmetric jet.

E. High viscosity of the outer fluid

Now we move to the cases where the outer fluid is more viscous than the inner fluid. Also in this regime, a small viscosity contrast increases the critical Reynolds number (Fig. 9), while for a large viscosity contrast the critical Reynolds number decreases. The reason for destabilization at high viscosity outside is however very different from the destabilization at low viscosity outside (described in the preceding section).

A space-time plot for $m = 10$ and $\mathrm{Re} = 250$ is shown in Fig. 16. This shows oblique fronts of convective instability. The visible front finally settles at a location around $x \approx 100$–120; however, the front is not stationary. The instability location is far downstream, although this jet, being more viscous, reaches a fully developed profile very quickly. Both features indicate that the instability is convective. When looking at logarithmically spaced contours (not shown), the instability is seen to grow monotonically from upstream to downstream until the location where it reaches a visible amplitude and saturates. The shape of the final oscillation (at $t = 1100$) is shown in Fig. 17. This shows a sinusoidal oscillation of large amplitude. A preliminary local stability analysis of these flows showed no absolute instabilities, but a very strong convective instability throughout the flow [with growth rates reaching $O(1)$ upstream], and the sinusoidal mode had a higher growth rate than the varicose mode. This agrees with our hypothesis that the instability observed at $m > 1$ is convective. It needs to

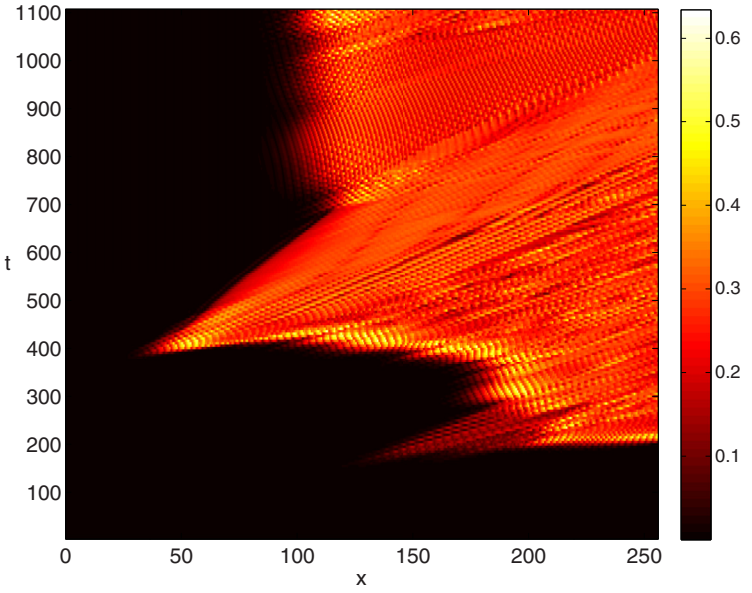

FIG. 16. Space-time diagram of the kinetic energy of the antisymmetric perturbation along the lines $y = \pm 1$, at $m = 10$ and $\mathrm{Re} = 250$. The downstream movement of the front in time shows that the instability occurs as convective bursts. This illustrates that the instability is convective (and not a global instability) for $m > 1$.

be remembered that also strong enough convective instabilities in noise-amplifier flows may persist nonlinearly without triggering. However, the parameters at which they persist will strongly depend on the level of numerical or experimental noise (cf. the boundary layer instability and transition).

F. Influence of the Weber number and the shear ratio

All results so far were computed with a fixer Weber number ($\mathrm{We} = 10$). It is worth considering qualitatively how the instability mechanisms change when the Weber number varies. To examine this, we have performed simulations at four selected viscosity ratios and four different Weber numbers. Figure 18(a) repeats the same results at $\mathrm{We} = 10$ for a visual reference.

We have not observed completely new instability mechanisms when We varies, but the neutral curves for each of the three modes described in the previous sections can move significantly. The most interesting effect is seen at low We (high surface tension), at low viscosity of the outer fluid.

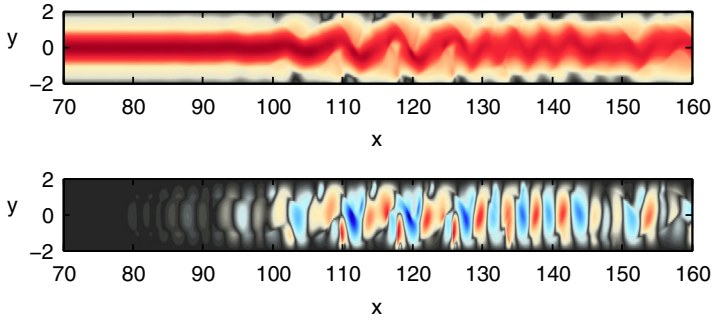

FIG. 17. Saturated sinusoidal oscillation of the jet at $m = 10$ and $\mathrm{Re} = 250$: streamwise velocity (top) and vertical velocity (bottom). Note that the vertical axis is magnified by a factor 3 compared to the horizontal axis.

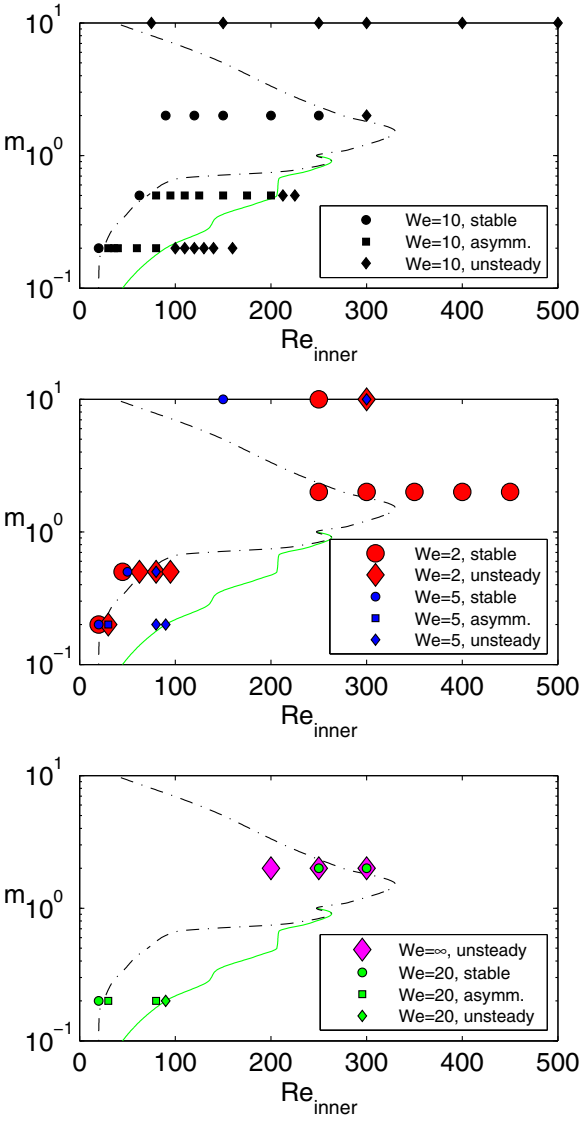

FIG. 18. Results from selected simulations at varying We (see the legend for exact values): We = 10 (top, reference), lower We (middle), and higher We (bottom). The meanings of the markers are as follows: ○, stable solution; □, steady asymmetric solution; and ◊, unsteady solution. Note that the unsteady solution is due to the surface-tension-induced mode at We = 2 and $m \leqslant 1$.

Figure 18(b) shows the simulation results at low We. At We = 2 (large red markers), the first bifurcation is directly time dependent. This can be seen from the round markers (stable flow) being adjacent to diamonds (unsteady flow). Inspection of the mode shapes [Figs. 19(a) and 19(b)] and the time signal [Fig. 19(c)] reveals that the first bifurcation in this case is due to the surface-tension-induced mode. The time signal is perfectly periodic and there is no sign of asymmetry. Furthermore, the mode shape is very similar to the low-Weber-number symmetric instability modes for jets (and wakes) found in global instability analyses [8,9]. The mode has a long wavelength and is localized close to the inlet.

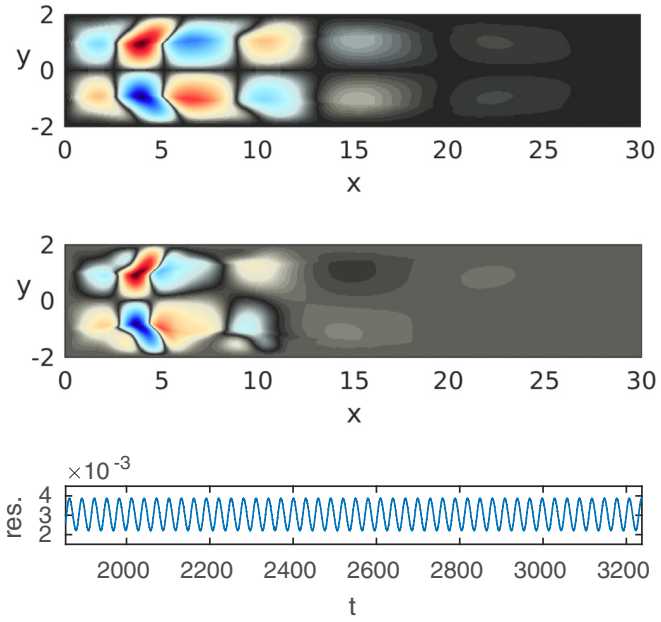

FIG. 19. First bifurcation by the surface-tension-induced mode at We = 0.5, for low viscosity of the outer fluid: vertical velocity for $m = 0.5$ and Re = 62.5 (top), vertical velocity for $m = 0.2$ and Re = 62.5 (middle), and saturated residual as a function of time for $m = 0.5$ and Re = 80 (bottom).

At We = 2, there is no indication of asymmetry (Coanda attachment) as there was at We = 10 [Fig. 18(a)], where round markers were followed by squares. This means that the whole bifurcation sequence is altered at high surface tension and suggests that there indeed is a mode competition when the viscosity of the outer fluid is low. At We = 10, the growth of the Coanda attachment mode leads to an asymmetric flow, which suppresses the surface-tension-induced mode. At We = 2, on the other hand, the surface-tension-induced mode is so strong that it prevents the Coanda mode from growing. The $m = 0.5$ and Re = 80 case [Fig. 19(a)] starts from the asymmetric steady flow at We = 10. Even in this case, the flow develops a surface-tension-induced mode oscillating around a symmetric mean. At We = 5 (slightly weaker surface tension), the first bifurcation is due to the surface-tension-induced mode at $m = 0.5$, but due to the Coanda attachment mode at $m = 0.2$. At We = 20 (much weaker surface tension), the first bifurcation is clearly due to the Coanda attachment mode. From this we conclude that the instability region for the surface-tension-induced mode grows constantly when We decreases to low enough values, at the expense of the Coanda mode. This is logical as Coanda attachment mode appears in single-phase flows, is related to the recirculation zones, and is unrelated to surface tension.

Let us now consider the flows with more viscous outer fluid. Figure 18(b) shows that at high values of surface tension (We = 2 and We = 5), the flow is significantly stabilized at both $m = 2$ and $m = 10$. Correspondingly, Fig. 18(c) shows that without surface tension (We = ∞), the flow is significantly destabilized at $m = 2$. Surface tension exerts the usual stabilizing influence on the oscillatory convective instability due to viscosity contrast. When the flow is initiated from an asymmetric steady solution, dissipative effects by surface tension are not important unless curvature is very large. Concluding, the surface-tension-induced global instability is likely to stabilize for high and low Weber numbers [9]. The other instability mechanisms remain, creating two separate instability regions for high-viscosity jets and low-viscosity jets, respectively. The most unstable viscosity contrast will be at very low viscosity of the outer fluid due to Coanda attachment.

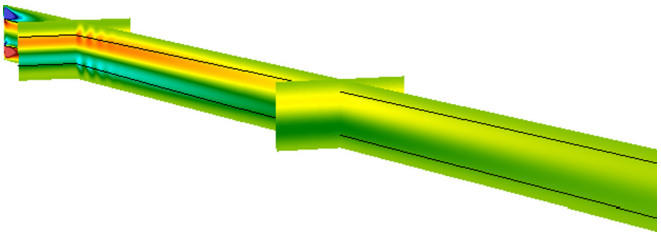

FIG. 20. Instantaneous vertical velocity from a three-dimensional direct numerical simulation at $m = 1$ and $\mathrm{Re} = 250$, shown together with the interface position (black line) at selected cross sections: $z = 0$, $x = 16$, and $x = 64$. The spanwise slices ($x = 16$ and $x = 64$) show that neither the velocity nor the interface position varies in the spanwise direction; the waves are fully two dimensional.

The influence of the shear ratio deserves brief consideration. A detailed parameter study on the surface-tension-induced global instability of uniform-viscosity jets was presented in Ref. [9]. There it was shown that increasing shear ratio (a stronger coflow at the inlet) was stabilizing for all Reynolds numbers studied ($\mathrm{Re} \leqslant 500$). However, the largest shear ratio at which the flow was globally unstable increased with increasing Reynolds number. We conclude that an increasing shear ratio should be always stabilizing for the surface-tension-induced mode. We also expect that the Coanda attachment mode is stabilized for high enough shear ratios, as a high coflow is likely to eliminate the recirculation zones at the walls. The convective instability at high viscosity of the outer fluid is not inflectional, but appears even in channel and Couette flows as well [1,3,5]. Hence, the instability at high viscosity of the outer fluid will not be qualitatively affected by changing shear ratio. In conclusion, an increasing shear ratio would stabilize except at high viscosity of the outer fluid and decreasing shear ratio would destabilize except at high viscosity of the outer fluid.

G. Absence of three dimensionality

We performed a selected number of three-dimensional direct numerical simulations to investigate whether three-dimensional effects could influence the instability onset or development. These studies were done at $\mathrm{We} = 10$ for three different viscosity ratios $m = 0.2$, 1, and 5 and three different Reynolds numbers $\mathrm{Re} = 125$, 175, and 250. The flow domain used was $[L_x, L_y, L_z] = [128,4,4]$ in the streamwise, vertical, and spanwise directions, respectively. The grid size was $N_x = 6094$ and $N_y = N_z = 128$, resulting in 67×10^6 grid points. The flow was run for several thousand nondimensional time units in each case.

The results showed without exception a two-dimensional flow field with a maximum spanwise velocity magnitude of 10^{-14}. A representative flow field from a three-dimensional direct numerical simulation is shown in Fig. 20. The spanwise cross sections show that the flow field remains fully two dimensional. These results imply that we can exclude three-dimensional effects on the instability boundaries and that secondary three-dimensional instabilities such as ligament formation are also unlikely in the investigated parameter regime. Previous studies have found ligament formation in viscosity-contrasted flows [13], but typically at a higher Weber number ($\mathrm{We} = 10$) and a higher viscosity ratio ($m = 30$). Here the surface tension is probably too strong to allow ligament formation. For low viscosity of the outer fluid, on the other hand, we might have expected a three-dimensional flow around the wall recirculation zones. However, it appears that the streamlines in our flows are not curved enough for centrifugal instabilities to form around the recirculation zones.

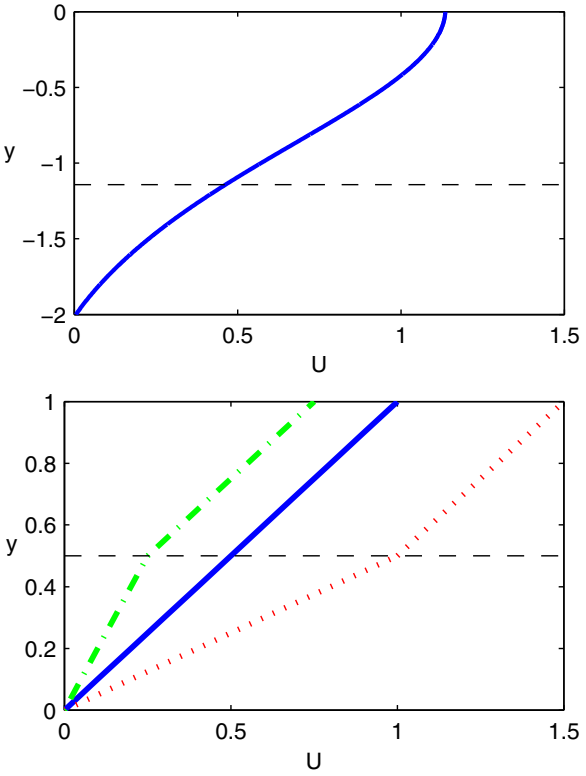

FIG. 21. Shown on top is the jet streamwise velocity profile from DNS at $m = 1$, Re $= 500$, and $x = 75$ (absolutely unstable due to surface tension), the lower half. On the bottom are the base flow profiles for the Couette model, at $m = 1$ (blue solid line), $m = 0.5$ (red dotted line), and $m = 2$ (green dash-dotted line). The problem is parametrized with respect to the shear of the upper layer.

V. PHYSICAL EXPLANATION FOR THE APPEARANCE AND DISAPPEARANCE OF THE SURFACE-TENSION-INDUCED INSTABILITY OF JETS

It has been predicted [7] that surface tension may promote absolute instability in inviscid shear layers where Kelvin-Helmholtz instability is already present. The destabilization of wakes by surface tension has been previously explained by an inviscid mechanism using a broken-line shear layer profile [10]. For wakes, the local and global instability is indeed located close to the inlet, where the velocity profile is strongly inflectional, and hence the destabilization of wakes could be explained by this model. However, jets have been observed to have convective instability due to surface tension for nearly parabolic profiles [9]. In the present work, also the absolute instability was seen to persist until $x > 70$ (Fig. 8), where the velocity gradient is nearly constant, as shown in Fig. 21. This suggests that the destabilization of jets could be due to another mechanism. The aim of the present section is to suggest a mechanism for the surface-tension-induced instability of jets and why it disappears when viscosity contrast is introduced. The aim is to give the simplest possible physical explanation for the neutral curve (Fig. 9).

Absolute instability can be seen as the counterpart of global instability in parallel flows (unless the instability mechanism itself requires a nonparallel flow, such as recirculation). To become absolutely unstable, the flow also needs to be temporally unstable (or, equivalently, convective instability precedes absolute instability). At uniform viscosity and in the absence of surface tension,

exactly one branch of local temporally unstable modes (here called the jet mode) exists for our jets. However, the jet mode never becomes absolutely unstable.

In the presence of surface tension, however, another branch of modes appears and becomes unstable, both convectively and absolutely. This second mode, the interfacial mode [9], is a hidden mode in any flow with uniform density and viscosity, which appears as a neutral line in the spectrum only if interfacial perturbations are considered. Since the interface has no influence on the flow without surface tension, the neutral line thus corresponds to a pure convection of the interfacial perturbation by the local mean flow: $\frac{\partial h}{\partial t} + U\frac{\partial h}{\partial x} = 0$. However, when even small surface tension or viscosity or density differences are introduced, the interface perturbation starts to interact with the flow and loses its neutral stability. We should point out that this is the same mode that is responsible for the Yih instability [3]. In that case, the interfacial mode described by Yih [3] as "a hidden neutral mode, ignored in conventional stability analyses," locally destabilizes Couette flow for all Reynolds numbers with even a minor viscosity contrast.

For jets, it is the interfacial mode that is responsible for the global instability [9] and it was hypothesized in Ref. [9] that the interaction of the two jet shear layers was not necessary but that the same instability could occur for a single shear layer. We now investigate this using the simplest possible model with the same main ingredients: shear, interfacial perturbation, viscosity gradient, and confinement. The model chosen is a Couette flow with a moving upper wall and two fluid layers occupying half of the channel each. A second reason for choosing this model system was to confirm that no inflection points are needed for surface-tension-induced instability: Only shear and surface tension are needed for the flow to become locally and globally unstable, as was hypothesized in Ref. [8]. This model also covers the mechanisms for Yih instability and short-wave instability and hence may shed light on what happens for viscosity-contrasted jets.

The Reynolds and Weber numbers are based on the shear and the channel height. The upper layer has more momentum and hence plays a role similar to the jet inner flow. The nondimensionalization is thus based on the parameters of the upper layer: $\mathrm{Re} = (dU/dy)_{\mathrm{up}}H^2$ and $\mathrm{Re} = (dU/dy)_{\mathrm{up}}H^2$. Note moreover that for $m = 1$ the velocity gradient for both layers is the same. Representative base flow profiles are shown in Fig. 21. The ansatz for the velocity, pressure, and interfacial perturbation is of the form

$$\mathbf{U}_{\mathrm{tot}} = \mathbf{U}_b(y) + \hat{\mathbf{u}}(x,y)\exp\{i\alpha x + \sigma t\}, \tag{5}$$

$$P_{\mathrm{tot}} = p(x,y)\exp\{i\alpha x + \sigma t\}, \tag{6}$$

$$h_{\mathrm{tot}} = 0.5 + \hat{h}\exp\{i\alpha x + \sigma t\}, \tag{7}$$

where $\mathbf{U}$ is the base flow velocity field, $\hat{u}(x,y)$ is the spatial shape of the velocity eigenmode, $\sigma = \sigma_r + i\sigma_i$ is the temporal eigenvalue ($\sigma_r > 0$ unstable), and α is the streamwise wave number. For these studies, we solve the same equations as in Ref. [9] using the FLUIDSPACK code, with the disturbance x derivatives replaced by $i\alpha$ and base flow x derivatives set to zero.

A. Destabilization by surface tension

For our jets, surface tension destabilizes a hidden interfacial mode both locally and globally. The Couette flow model without Kelvin-Helmholtz instability reproduces the latter behavior. The critical shear-based Reynolds numbers for the onset of convective and absolute instability are shown in Fig. 22 for varying Weber numbers.

Let us first analyze the convective instability. The local temporal (i.e., convective) instability spectrum for an unstable case ($\mathrm{We} = 25$, $\mathrm{Re} = 1300$, and $m = 1$) is shown in Fig. 23 for varying α_r. Two unstable modes appear, with exactly the same growth rate for the same α_r, but with different phase speeds. The eigenmode shape of the slower mode (M1) at the wavelength corresponding to instability maximum ($\alpha_r = 2.7$) is shown in Fig. 24. The kinetic energy of the M1 mode is symmetrically distributed above and below the interface (at $y = 0.5$). The faster mode (M2) has a

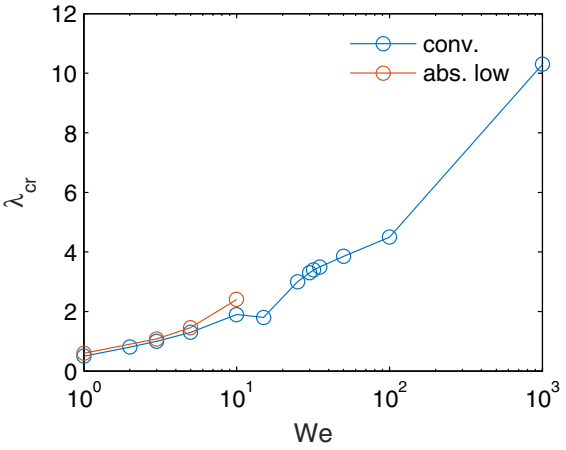

FIG. 22. Critical Reynolds number for the onset of instability (convective and absolute) with surface tension, for the Couette flow model. The upper limit for absolute instability is also depicted (convective instability exists for all finite $\mathrm{Re} > \mathrm{Re}_{cr}$).

similar shape but its amplitude maximum is located in the faster fluid, and due to this it seems to have a higher group velocity and never becomes absolutely unstable. Here we focus on the slower mode (M1), because it also has the lowest group velocity and is the one that becomes absolutely unstable.

Mode M1 is present for all Reynolds numbers above a critical threshold. We have analysed values up to $\mathrm{Re} = 500\,000$. However, the growth rate decays towards zero for high Reynolds numbers. Consequently, surface tension destabilizes the interfacial mode by a viscous mechanism. We can analyze this further by separating the components that cause growth of the perturbation kinetic energy. The normalized kinetic energy of an eigenmode $E_{\mathrm{kin}}^{-1}(dE_{\mathrm{kin}}/dt)$ grows or decays at the same rate as the mode. Hence the components of this expression can be used to analyze how different mechanisms contribute to the eigenvalue growth. The perturbation kinetic energy equation (derived

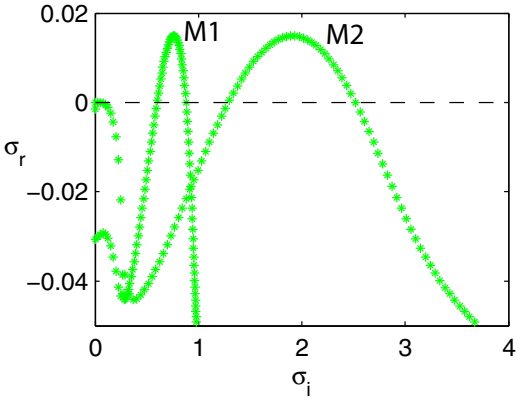

FIG. 23. Eigenvalue spectrum (all wave numbers) for the two-fluid Couette flow model, at $m = 1$, $\mathrm{We} = 25$, and $\mathrm{Re} = 1300$. Two unstable modes are shown.

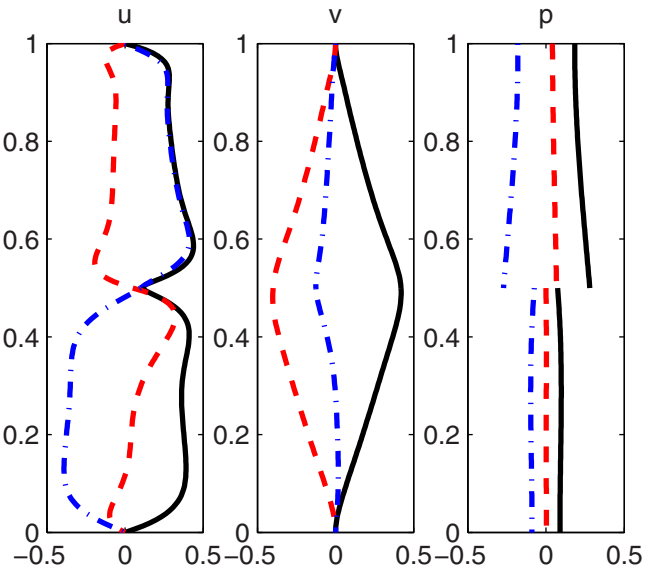

FIG. 24. Eigenfunction for the slower unstable (interfacial) mode.

in Appendix A) becomes

$$\frac{dE_{\text{kin}}}{dt} = \int^{(1),(2)} \frac{\partial \|\mathbf{u}\|^2}{\partial t}$$
$$= \int^{(1),(2)} -(u^* v + v^* u)U' + \int^{(1)} -\frac{2}{\text{Re}}(\|\alpha \mathbf{u}\|^2 + \|D\mathbf{u}\|^2)$$
$$+ \int^{(2)} -\frac{2m}{\text{Re}}(\|\alpha \mathbf{u}\|^2 + \|D\mathbf{u}\|^2) + W_{\text{We}} + W_m, \tag{8}$$

where the work performed by the surface tension is

$$W_{\text{We}} = \int_B -\frac{\alpha^2}{\text{We}} \frac{\partial \|h\|^2}{\partial t} \tag{9}$$

and the work performed by viscosity contrast at the interface is

$$W_m = \int_B \frac{(m-1)}{m\,\text{Re}} [2\alpha^2 U \|h\|^2 + Du^{(1)} h^* + Du^{(1)*} h]. \tag{10}$$

The sign of each integral component tells us whether it is stabilizing or destabilizing and their relative magnitudes can be compared as well. The first volumetric integral is the well-known kinetic energy production by base flow shear and the second and third integrals are the viscous dissipation in each domain. The surface term W_{We} is the energy dissipation due to surface tension. This term is negative whenever the eigenmode growth is positive; it is known that surface tension in itself cannot destabilize parallel flows. The surface term W_m is the energy production due to a viscosity contrast, which is zero for $m = 1$. This means that the surface-tension-induced (temporal) instability must be due to the volumetric terms: the energy production and dissipation inside the domain. It is known that inviscid flows cannot have kinetic energy production (from the base flow shear) without inflection point and hence it is only logical that the surface-tension-induced instability is viscous.

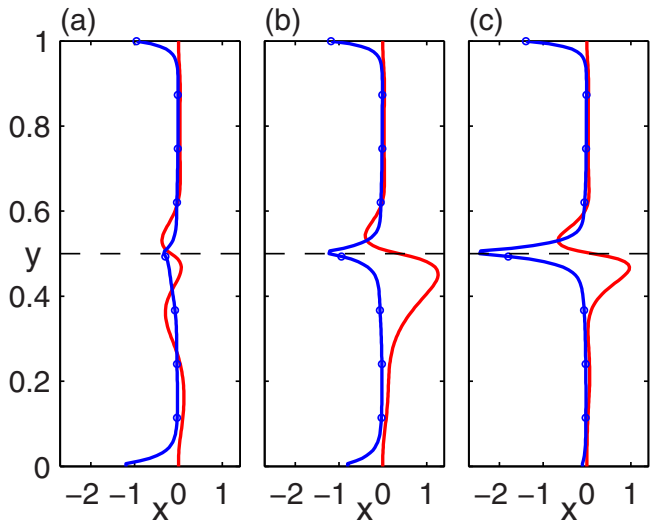

FIG. 25. Vertical distribution of the production (red solid line) and dissipation (blue dash-dotted line) of kinetic energy for the eigenmode at $m = 1$, $\mathrm{Re} = 1300$, $\alpha_r = 2.7$, and (a) $\mathrm{We} = 100$ ($\sigma_r = -0.05$), (b) $\mathrm{We} = 25$ ($\sigma_r = 0.02$), and (c) $\mathrm{We} = 10$ ($\sigma_r = -0.02$). The surface position is shown by a black dashed horizontal line.

The magnitudes of the three terms can be compared to each other for M1. For the unstable cases, production and dissipation are both larger than the term due to surface tension. For instance, at $\mathrm{We} = 25$ (the most unstable Weber number in Fig. 22) at $\mathrm{Re} = 1300$ and $\alpha = 2.7$ (the most unstable wave number for this case), the magnitudes are 0.18 for production, -0.13 for viscous dissipation, and -0.026 for dissipation by surface tension. The vertical distribution of production and dissipation is shown in Fig. 25 for $\mathrm{We} = 100$ [Fig. 25(a)], $\mathrm{We} = 25$ [Fig. 25(b)], and $\mathrm{We} = 10$ [Fig. 25(c)]. This shows that at low surface tension [Fig. 25(a)], there is not much production or dissipation. When the surface tension increases to $\mathrm{We} = 25$ [Fig. 25(b)], there is efficient energy production in the slower fluid and some dissipation at the surface. When the surface tension increases further [Fig. 25(c)], the production decreases while the dissipation near the surface increases. In conclusion, the right amount of surface tension destabilizes the M1 mode by regulating the delicate balance between production and dissipation and the dissipation by surface tension itself is negligible in comparison to this effect.

Based on these figures, the instability mechanism might be hypothesized as follows. A wavelike perturbation of the interface induces a wavelike perturbation of pressure in order to satisfy the stress balance in the presence of surface tension. The streamwise pressure gradients in turn induce a streamwise velocity perturbation and vertical velocity perturbation by mass conservation. This is the flow that pulls the interface back to its flat position. Considering a stationary situation, a perturbation that pulls the interface back must be symmetric with respect to the interface for the vertical and antisymmetric for the streamwise velocity. Figure 24 shows that M1 has this symmetry property and Fig. 4 shows clearly that the jet global mode has this symmetry as well. This tendency to pull the interface back results in a situation where u and v have opposite signs in the slower fluid, which makes it possible to extract energy from the mean shear in the slower fluid. The presence of viscosity makes it possible to extract energy through the term $-uvU'$ even without inflection points; however, near the surface the mode experiences a high level of viscous dissipation at the surface because of the steep gradient of the mode du/dy. Surface tension dictates the vertical scale of M1: A high surface tension focuses the mode close to the surface, resulting in high viscous dissipation near the surface [Fig. 25(c)], while a low surface tension results in a weaker mode with neither

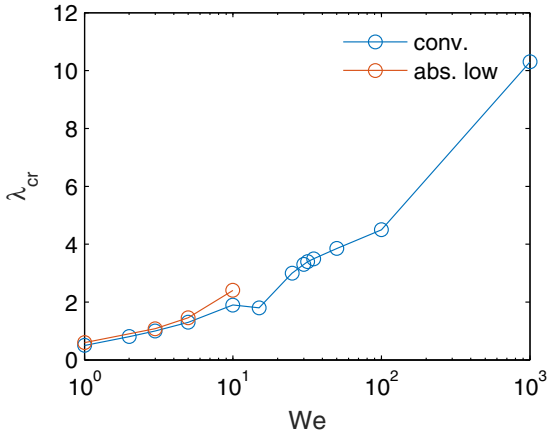

FIG. 26. Wave number at the onset of instability (convective and absolute) with surface tension, for the Couette flow model.

production nor dissipation [Fig. 25(c)]. Intermediate surface tension [Fig. 25(b)] allows the mode to penetrate deep enough into the lower fluid to have efficient production while keeping the surface gradients moderate.

Finally, surface tension introduces damping and hence slows down the oscillation frequency. As waves of high wave numbers have higher curvature, they seem to be slowed down by surface tension more than low wave numbers. Near capillary wavelength, the change in phase speed $c = \omega/k$ is particularly rapid and this may result in unstable waves with zero group speed. In an inviscid Kelvin-Helmholtz shear layer [7], surface tension induced absolute instability. Here we show that in the Couette model system without inflection points, surface tension induces an absolute instability of M1 (the red lines in Fig. 22). This happens only when surface tension is strong enough at low Weber numbers (We < 15). The critical (lowest) Reynolds number at which the absolute instability appears is a function of the Weber number. However, there is also a highest Reynolds number above which the absolute instability disappears.

Extrapolating this information from M1 to the observed jet mode with the same structure, we hypothesize that the global surface-tension-driven instability is viscous and disappears when the Reynolds number is increased. Finally, the wave number at the onset of convective and absolute instability is depicted in Fig. 26. The convective and absolute instabilities of the interfacial mode appear at similar wave numbers and the wave number α_{cr} at the instability onset increases with Weber number.

B. Effect of a viscosity ratio

Now a viscosity ratio is introduced while keeping the shear-based Reynolds number of the upper layer constant. Figure 27 shows how the frequency and growth of the two interfacial modes (M1 and M2) changes at We $= 25$ and Re $= 1300$, when a viscosity ratio is introduced. The green line shows the $m = 1$ case.

The blue markers in Fig. 27 show M1 and M2 with a less viscous outer fluid ($m = 0.8$). The growth of M1 is slightly smaller than for $m = 1$. The main change, however, is that the phase velocity of M1 (and M2) increases considerably. This is because M1 travels at the surface velocity and the surface velocity increases to satisfy the base flow stress balance (Fig. 21). This increase of the convection velocity happens also for the jet. It turns out that this increases the group velocity of the mode. Absolute instability is weakened and seems to disappear for viscosity ratios $m < 0.7$. In the DNS, we observed an unstable stationary Coanda global mode. However, the Coanda mode is

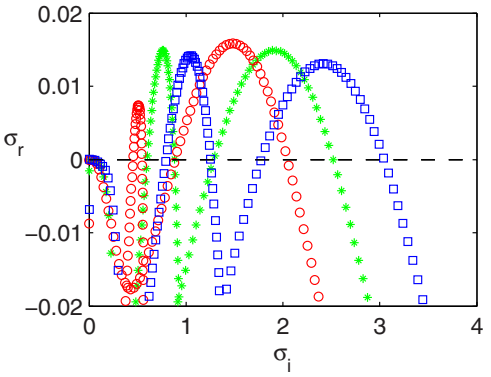

FIG. 27. Eigenvalue spectrum (all wave numbers) for the two-fluid Couette flow model, at different viscosity ratios, We = 25, Re = 1300, and $m = 1$ (uniform viscosity) (green stars), $m = 1.3$ (high viscosity in the slower fluid) (red circles), and $m = 0.8$ (low viscosity in the slower fluid) (blue squares).

not due to local absolute instability, but requires an essentially nonparallel flow (it strongly depends on the size of a closed recirculation zone). Hence, we cannot observe Coanda instability in the Couette model. However, the Couette model predicts that the surface-tension-induced instability should stabilize at low outer fluid viscosity, which agrees with our observations from the DNS.

The red markers in Fig. 27 show M1 and M2 with a more viscous outer fluid ($m = 1.3$). Now both modes have slowed down because the interfacial velocity has decreased. However, the growth rate of M1 has halved. We have done an energy analysis at the point of maximum growth of M1, which is still at $\alpha = 2.7$. This reveals that the energy production by base flow shear (0.17) is slightly smaller than in the uniform viscosity case and there is more viscous dissipation: -0.16. The energy dissipation due to surface tension is -0.014 and the energy production by viscosity contrast 0.014. Hence, the surface terms take each other out and their contributions are an order of magnitude smaller compared to the volumetric terms; the stability is regulated by the balance between production by the base flow shear and viscous dissipation. The production and dissipation distributions are shown in Fig. 28, illustrating that viscous dissipation increases for $m > 1$ both near the surface and in the more viscous fluid. The decrease of the temporal growth of M1 also pushes the zero-group-velocity point to the stable half plane; for $m > 1$, the absolute instability of M1 soon disappears. It is interesting to note that the growth rate of M2 actually increases. However, M2 does not become absolutely unstable because of its high convection speed. This could explain the strong convective instability of the jets at $m > 1$.

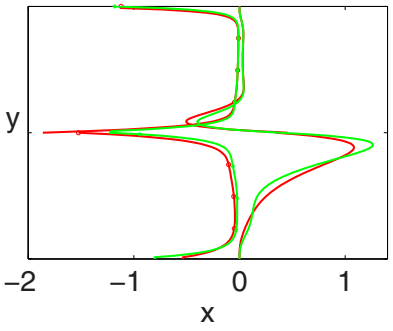

FIG. 28. Production (plain solid line) and dissipation (line with markers) distributions, as in Fig. 25, for the interfacial mode at $m = 1$ (green) and $m = 1.3$ (red).

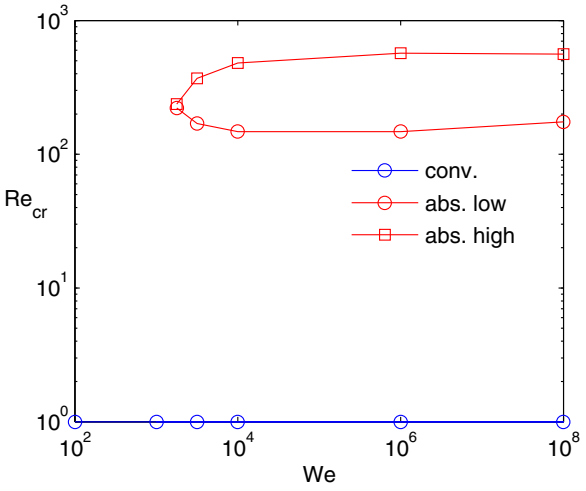

FIG. 29. Same as Fig. 22 but for viscous outer fluid at $m = 10$. The flow is convectively unstable for all Re through the Yih mechanism. (Re = 1 was the lowest Reynolds number tested.)

Summarizing, the viscosity ratio differs from unity, in either direction, and the surface-tension-driven absolute instability soon disappears. Most cases with lower viscosity of the outer fluid do not have any absolute instability. The cases with high viscosity outside show that the neutral curve displays a very strong convective instability. The convective and absolute instabilities for $m = 10$ are shown in Fig. 29. The flow is convectively unstable for all Reynolds numbers as expected by the Yih and shortwave instability mechanisms (the lowest Reynolds number tried here was Re = 1). The case $m = 10$ depicts some absolute instability, but with the opposite trend compared to surface-tension-driven instability: The absolute instability appears only at very high Weber numbers. This shows that the absolute instability mechanism is viscosity driven, stabilized by surface tension. Extrapolating this information to our jet, the shear-based Weber numbers are so high that our jet at $m = 10$ is not likely to have any absolute instability. However, at even higher viscosity ratios, the absolute instability is moved to lower Weber numbers in this Couette model. At $m = 30$, the Couette flow is absolutely unstable at Re = 100, similarly to the viscous liquid layer by [13]. Hence, while the high-viscosity cases presented in this paper are convective, if the viscosity ratio of the jet is increased even more, we are likely to observe another mode of global instability.

VI. CONCLUSION

In this study we have investigated how the viscosity ratio influences the global instability of an immiscible confined coflow jet, by direct numerical simulations of the two-fluid system using a level-set method. The main focus has been to quantify how the surface-tension-induced instability of jets is influenced by a viscosity contrast. We find that a small viscosity contrast in both directions is stabilizing, while at larger viscosity contrasts the critical Reynolds number is decreased due to other instability mechanisms that take over at high viscosity contrast. The instability mechanisms were further analyzed using time-space diagrams.

For a coflow of less viscous fluid outside the jet, when the Reynolds number is increased from zero, the first bifurcation is through a Coanda attachment instability, which makes the jet steady but asymmetric. This is because recirculation zones develop in the less viscous outer phase and the length of these zones increases as a function of viscosity contrast, further decreasing the critical Reynolds number. When Reynolds number is increased, time-dependent convective bursts develop

particularly around the larger recirculation zone. For a coflow of more viscous fluid outside the jet, the first bifurcation is through a very strong convective instability that appears in the unforced DNS.

Finally, we analyzed the origin of the local and global destabilization of a hidden interfacial mode in the jet flow by means of local stability analysis of a two-layer Couette flow model system. We show that a qualitatively similar local and global destabilization by surface tension is obtained for Couette flow and that the mode is viscous (vanishes in inviscid flow). We show that the absolute instability occurs at uniform viscosity but vanishes with lower viscosity of the outer flow (due to increase of interfacial convection speed) and with higher viscosity of the outer flow (the mode extracts its energy in the slower fluid). The viscous instability mechanism found here occurs without inflection points and is different from the inviscid mechanism found by [10] in immiscible wake flows (by interaction between a Rossby wave at a vorticity discontinuity and a capillary wave). The viscous mechanism could explain the destabilization of these jets, particularly as nearly parabolic [9] and constant-gradient jet profiles were destabilized in this work. However, both mechanisms can exist or coexist for jets and wakes for different parameter regimes.

ACKNOWLEDGMENTS

The work of O.T. received financial support from the Swedish Research Council through Grant No. VR2013-5789. J.-C.L. and L.B. acknowledge support from the European Research Council Grant No. ERC-2013-CoG-616186, TRITOS, and the Swedish Research Council. The authors acknowledge computer time provided by the Swedish National Infrastructure for Computing at PDC Centre for High Performance Computing. The authors also wish to thank Lennon Ó Náraigh for introducing them to the TPLS solver.

APPENDIX A: DERIVATION OF THE PERTURBATION KINETIC ENERGY GROWTH

For an unstable local linear eigenmode, the kinetic energy and the interfacial energy both grow at the same (exponential) rate. Hence, to find mechanisms of eigenvalue growth we may choose to focus on the kinetic energy, because $\sigma_r = (1/E_{\mathrm{kin}})\frac{d}{dt}(E_{\mathrm{kin}})$,

$$\int u_i \frac{\partial u_i}{\partial t} + \int u_i U_j \frac{\partial u_i}{\partial x_j} + \int u_i u_j \frac{\partial U_i}{\partial x_j} + \int u_i u_j \frac{\partial u_i}{\partial x_j} = \int u_i \frac{\partial \tau_{ij}}{\partial x_j}, \tag{A1}$$

where $\tau_{ij} = -p\delta_{ij} + (1/\tilde{\mathrm{Re}})(\frac{\partial u_i}{\partial x_j} + \frac{\partial u_j}{\partial x_i})$ and $\tilde{\mathrm{Re}} = \mathrm{Re}$ in region 1 and $\tilde{\mathrm{Re}} = \mathrm{Re}/m$ in region 2. This can be partially integrated at each of the two regions separated by the steady positions of the interface to yield

$$\begin{aligned}
&\int \frac{1}{2}\frac{\partial (u_i u_i)}{\partial t} + \int \frac{1}{2}\frac{\partial (u_i u_i U_j + u_i u_i u_j)}{\partial x_j} + \int u_i u_j \frac{\partial U_i}{\partial x_j} \\
&\quad = \int \frac{\partial}{\partial x_j}\left\{ u_i \left[-p\delta_{ij} + \tilde{\mathrm{Re}}^{-1}\left(\frac{\partial u_i}{\partial x_j} + \frac{\partial u_j}{\partial x_i}\right)\right]\right\} + \int p\frac{\partial u_i}{\partial x_i} - \int \frac{\partial u_i}{\partial x_j}\tilde{\mathrm{Re}}^{-1}\left(\frac{\partial u_i}{\partial x_j} + \frac{\partial u_j}{\partial x_i}\right) \\
&\quad = \int_B [u_i \tau_{ij} N_j] - \int \tilde{\mathrm{Re}}^{-1}\frac{\partial u_i}{\partial x_j}\frac{\partial u_i}{\partial x_j} - \int \frac{\partial}{\partial x_j}\left[\tilde{\mathrm{Re}}^{-1} u_i \frac{\partial u_j}{\partial x_i}\right] + \int \tilde{\mathrm{Re}}^{-1} u_i \frac{\partial^2 u_j}{\partial x_i \partial x_j} \\
&\quad = -\int \tilde{\mathrm{Re}}^{-1}\frac{\partial u_i}{\partial x_j}\frac{\partial u_i}{\partial x_j} + \int_B [u_i \tau_{ij} N_j] - \int_B \left[\tilde{\mathrm{Re}}^{-1} u_i \frac{\partial u_j}{\partial x_i} N_j\right],
\end{aligned} \tag{A2}$$

where N_j is the outward pointing normal of the steady interface and several terms were eliminated by applying the continuity equation for the base flow and the perturbation. Hence, this gives the following equation for the evolution of perturbation kinetic energy in each of the two regions:

$$\int \frac{1}{2}\frac{\partial(u_i u_i)}{\partial t} = \int -u_i u_j \frac{\partial U_i}{\partial x_j} + \int -\tilde{\mathrm{Re}}^{-1}\frac{\partial u_i}{\partial x_j}\frac{\partial u_i}{\partial x_j} + \int_B \left[-\frac{1}{2}(u_i u_i U_j + u_i u_i u_j)N_j\right] + \int_B [u_i \tau_{ij} N_j] + \int_B \left[-\tilde{\mathrm{Re}}^{-1} u_i \frac{\partial u_j}{\partial x_i} N_j\right], \tag{A3}$$

where N_i is the outward pointing normal from each domain. The first term is the well-known energy production in shear flows and the second dissipation due to viscosity (which is always negative). The rest are transport terms, which vanish at outer boundaries, but not necessarily at the interface between the two fluids.

In the Couette flow problem, we have $\mathbf{U}^{(1)} = [y + (m-1)/2m, 0]$ in the upper domain and $\mathbf{U}^{(2)} = (y/m, 0)$ in the lower domain, which gives $U'^{(1)} = 1, U'^{(2)} = 1/m, N^{(2)} = (0,-1)$, and $N^{(1)} = (0,1)$. Summing these up, the total rate of change of kinetic energy in the (Couette flow) system becomes

$$\begin{aligned}\int^{(1),(2)} \frac{1}{2}\frac{\partial(uu+vv)}{\partial t} = {} & \int^{(1),(2)} -uvU' + \int^{(1)} -\frac{1}{\mathrm{Re}}\left(\frac{\partial u}{\partial x}\frac{\partial u}{\partial x} + \frac{\partial u}{\partial y}\frac{\partial u}{\partial y} + \frac{\partial v}{\partial x}\frac{\partial v}{\partial x} + \frac{\partial v}{\partial y}\frac{\partial v}{\partial y}\right) \\ & + \int^{(2)} -\frac{m}{\mathrm{Re}}\left(\frac{\partial u}{\partial x}\frac{\partial u}{\partial x} + \frac{\partial u}{\partial y}\frac{\partial u}{\partial y} + \frac{\partial v}{\partial x}\frac{\partial v}{\partial x} + \frac{\partial v}{\partial y}\frac{\partial v}{\partial y}\right) \\ & - \int_B \Delta\left[\frac{1}{2}(uu+vv)v\right] + \int_B \Delta[u\tau_{12} + v\tau_{22}] \\ & + \int_B \left[-\frac{m}{\mathrm{Re}}\left(u^{(2)}\frac{\partial v^{(2)}}{\partial x} + v^{(2)}\frac{\partial v^{(2)}}{\partial y}\right) + \frac{1}{\mathrm{Re}}\left(u^{(1)}\frac{\partial v^{(1)}}{\partial x} + v^{(1)}\frac{\partial v^{(1)}}{\partial y}\right)\right].\end{aligned} \tag{A4}$$

We are interested in the time-averaged kinetic energy growth of a local stability eigenmode over a period $T = 2\pi/\omega$ and a wavelength $\lambda = 2\pi/\alpha$. From now on, all integrals should be interpreted as such averages. The complex temporal modal ansatz for the local analysis is

$$u(x,y,t) = \mathrm{Re}\{\hat{u}(y)\exp(i\alpha x + \sigma t)\} = \tfrac{1}{2}[\hat{u}(y)\exp(i\alpha x + \sigma t) + \hat{u}(y)^*\exp(-i\alpha x + \sigma^* t)] \tag{A5}$$

and similarly for other variables. The real quantities can be obtained by the transformation $\mathrm{Re}\{u\} = \frac{1}{2}(u + u^*)$, where the asterisk denotes a complex conjugate. The average over T and λ means that only the products of one nonconjugated and one conjugate variable survive the integration, whereas products of an odd number of perturbation variables do not. This means that the first boundary term will cancel. Furthermore, the boundary terms containing Re will cancel due to continuity. Finally,

we obtain

$$\int^{(1),(2)} \frac{\partial(u^*u + v^*v)}{\partial t}$$
$$= \int^{(1),(2)} -(u^*v + v^*u)U' + \int^{(1)} -\frac{2}{\mathrm{Re}}[\alpha^2(u^*u + v^*v) + Du^*Du + Dv^*Dv]$$
$$+ \int^{(2)} -\frac{2m}{\mathrm{Re}}[\alpha^2(u^*u + v^*v) + Du^*Du + Dv^*Dv] + \int_B \Delta[u^*\tau_{12} + u\tau_{12}^* + v^*\tau_{22} + v\tau_{22}^*], \tag{A6}$$

where $\Delta f = f^{(2)} - f^{(1)}$ denotes the jump of f over the interface. Let us develop the remaining boundary term further. We define $N^{(2)} = N$ and $n^{(2)} = n$ in what follows. The kinematic and dynamic interfacial conditions are (compare to [9], where the domains are interchanged)

$$\Delta u = -h\Delta U', \quad \Delta v = 0, \tag{A7}$$

$$N_j\Delta\tau_{ij} + n_j\Delta\mathcal{T}_{ij} + N_j h\Delta\frac{\partial\mathcal{T}_{ij}}{\partial y} = \mathrm{We}^{-1}\left(\frac{\partial N_j}{\partial x_j}n_i + \frac{\partial n_j}{\partial x_j}N_i\right). \tag{A8}$$

For the Couette problem, the second (dynamic) condition simplifies to

$$\Delta\tau_{12} = 0, \quad \Delta\tau_{22} = \mathrm{We}^{-1}\frac{\partial n_j}{\partial x_j}. \tag{A9}$$

As $\mathbf{n} = (-i\alpha h, 0)$ and $\Delta U' = (1-m)/m$, we obtain

$$\begin{aligned}
&\Delta[u^*\tau_{12}+v^*\tau_{22}+u\tau_{12}^*+v\tau_{22}^*] \\
&= [\tau_{12}\Delta u^* + \tau_{12}^*\Delta u] + \frac{1}{2}[v^*\Delta\tau_{22} + v\Delta\tau_{22}^*] \\
&= \frac{1}{\mathrm{Re}}[(i\alpha v + Du^{(1)})\Delta u^* + (i\alpha v + Du^{(1)})^*\Delta u] - \frac{\alpha^2}{\mathrm{We}}(v^*h + vh^*) \\
&= \frac{m-1}{m\,\mathrm{Re}}[(i\alpha v + Du)h^* + (-i\alpha v^* + Du^*)h] - \frac{\alpha^2}{\mathrm{We}}(v^*h + vh^*) \\
&= \frac{(m-1)}{m\,\mathrm{Re}}[i\alpha(vh^* - v^*h) + (h^*Du + hDu^*)] - \frac{\alpha^2}{\mathrm{We}}(v^*h + vh^*)
\end{aligned} \tag{A10}$$

and similarly for the complex conjugate of this expression. Further, we can make use of the interface kinetic condition

$$\frac{\partial h}{\partial t} + i\alpha Uh = v, \tag{A11}$$

which gives

$$v^*h + h^*v = \left(h^*\frac{\partial h}{\partial t} + h\frac{\partial h^*}{\partial t}\right) = \frac{\partial(h^*h)}{\partial t} \tag{A12}$$

and

$$v^*h - h^*v = \left(h^*\frac{\partial h}{\partial t} - h\frac{\partial h^*}{\partial t}\right) = 2i\alpha U h^*h. \tag{A13}$$

Summary. We have arrived at the final energy equation

$$\begin{aligned}\frac{dE_{\text{kin}}}{dt} &= \int^{(1),(2)} \frac{\partial\|\mathbf{u}\|^2}{\partial t} \\ &= \int^{(1),(2)} -(u^*v + v^*u)U' + \int^{(1)} -\frac{2}{\text{Re}}(\|\alpha\mathbf{u}\|^2 + \|D\mathbf{u}\|^2) \\ &\quad + \int^{(2)} -\frac{2m}{\text{Re}}(\|\alpha\mathbf{u}\|^2 + \|D\mathbf{u}\|^2) + W_{\text{We}} + W_m,\end{aligned} \tag{A14}$$

where the work performed by the surface tension is

$$W_{\text{We}} = \int_B -\frac{\alpha^2}{\text{We}}\frac{\partial\|h\|^2}{\partial t} \tag{A15}$$

and the work performed by viscosity contrast at the interface is

$$W_m = \int_B \frac{m-1}{m\,\text{Re}}[2\alpha^2 U\|h\|^2 + Du^{(1)}h^* + Du^{(1)*}h]. \tag{A16}$$

The growth rate of the eigenmode can be recovered from $E_{\text{kin}}^{-1}(dE_{\text{kin}}/dt)$ and hence the components of this expression can be used to analyze how different mechanisms contribute to the eigenvalue growth (the sign tells us whether it is stabilizing or destabilizing and their relative magnitudes can be compared as well).

The work performed by viscosity contrast may be both positive or negative, depending on the sign of the viscosity contrast ($m < 1$ or $m > 1$) and the relation between $Du^{(1)}$ and h. The work performed by surface tension has a negative sign; as is known, surface tension in itself is purely dissipative in a local temporal sense. However, in the present paper it was shown that the surface tension invokes streamwise and vertical velocities near the surface and when these two are appropriate phase difference they will extract energy from the mean flow shear even without inflection points, similarly to Tollmien-Schlichting waves in boundary layers.

APPENDIX B: SUMMARY OF THE SIMULATION PARAMETERS

The following meshes have been used in the nonlinear simulations, all having the same grid spacing. Mesh M1 has 1 024 000 grid points, domain length $L = 250$, and grid spacing 0.0078 times the channel diameter, resulting in x degrees of freedom. Mesh M2 has 1 966 080 grid points, domain length $L = 120$, and grid spacing 0.0039 times the channel diameter, resulting in x degrees of freedom. Mesh M3 has 4 096 000 grid points, domain length $L = 250$, and grid spacing 0.0039 times the channel diameter, resulting in x degrees of freedom. Tables I–VII summarize the simulation parameters.

TABLE I. Simulation parameters, $m = 0.1$–0.3333, and $\mathrm{We} = 10$.

m	$\mathrm{Re}_{\mathrm{inner}}$	Grid	L	T_{DNS} $(+T_{sfd})$	ΔT	From steady?	Final residual (average time)	Final state
0.1	40	M2	120	1189 (+626)	1×10^{-3}	yes	5.2×10^{-6} (100)	asymmetric steady
0.1	50	M2	120	2259 (+621)	1×10^{-3}	yes	9.8×10^{-4} (100)	unsteady
0.1	60	M2	120	1305	1×10^{-3}	no	6×10^{-3} (100)	unsteady
0.1	70	M2	120	842	1×10^{-3}	no	7.6×10^{-3} (100)	unsteady
0.1	80	M2	120	814	1×10^{-3}	no	2.7×10^{-2} (93)	unsteady
0.1	90	M2	120	1568	1×10^{-3}	no	3.7×10^{-2} (90)	unsteady
0.1	100	M2	120	821	1×10^{-3}	no	4.5×10^{-2} (100)	unsteady
0.1	200	M2	120	498	1×10^{-3}	no	1×10^{-1} (94)	unsteady
0.1667	25	M1	250	2890	5×10^{-3}	no	2.0×10^{-8} (100)	symmetric steady
0.1667	25	M1	250	1979 (+686)	2.5×10^{-3}	yes	2.0×10^{-8} ($A = 4 \times 10^{-10}$) (100)	symmetric steady
0.1667	25	M1	250	2366 (+3206)	2.5×10^{-3}	yes ($\mathrm{Re} = 37.5$)	2.1×10^{-6} ($A = 3 \times 10^{-6}$) (100)	asymmetric steady
0.1667	37.5	M1	250	2555 (+1263)	2.5×10^{-3}	yes	5.0×10^{-5} ($A = 9 \times 10^{-4}$) (100)	asymmetric steady
0.1667	37.5	M1	250	3425	5×10^{-3}	no	2.0×10^{-7} (100)	asymmetric steady
0.1667	45.8	M1	250	2000 (+1000)	5×10^{-3}	yes	2.0×10^{-8} (100)	asymmetric steady
0.1667	53.3	M1	250	2000 (+2000)	5×10^{-3}	yes	1.8×10^{-8} (100)	asymmetric steady
0.1667	66.7	M1	250	3904 (+2000)	5×10^{-3}	yes	1.5×10^{-5} ($A = 3 \times 10^{-8}$) (100)	asymmetric steady
0.1667	83.3	M1	250	4712 (+2000)	5×10^{-3}	yes	3.3×10^{-4} (100)	unsteady
0.2	20	M1	250	501	1×10^{-3}	yes ($\mathrm{Re} = 36$)	2.3×10^{-8} ($A = 3 \times 10^{-11}$) (100)	symmetric steady
0.2	30	M1	250	891	1×10^{-3}	no	2.1×10^{-8} (100)	symmetric steady
0.2	30	M1	250	1247 (+500)	2.5×10^{-3}	yes	1.9×10^{-8} ($A = 1 \times 10^{-13}$) (100)	symmetric steady
0.2	30	M1	250	1014 (+2639)	2.5×10^{-3}	yes ($\mathrm{Re} = 36$)	2.1×10^{-7} ($A = 3 \times 10^{-5}$) (100)	asymmetric steady
0.2	36	M1	250	2639 (+4642)	2.5×10^{-3}	yes ($\mathrm{Re} = 40$)	1.5×10^{-5} ($A = 2 \times 10^{-7}$) (100)	asymmetric steady
0.2	40	M1	250	3632 (+1000)	2.5×10^{-3}	yes	1.1×10^{-5} (100)	asymmetric steady
0.2	50	M1	250	3405 (+1000)	2.5×10^{-3}	yes	2.0×10^{-6} (100)	asymmetric steady
0.2	80	M1	250	3205 (+1281)	2.5×10^{-3}	yes	2.9×10^{-8} (100)	asymmetric steady
0.2	100	M1	250	5005 (+660)	2.5×10^{-3}	yes	2.2×10^{-5} (100)	unsteady
0.2	110	M1	250	5657	5×10^{-3}	no	8.3×10^{-3} (100)	unsteady
0.2	120	M1	250	2000	5×10^{-3}	no	1.4×10^{-2} (100)	unsteady
0.2	140	M1	250	1998	5×10^{-3}	no	2.0×10^{-2} (100)	unsteady
0.2	160	M1	250	1000	5×10^{-3}	no	2.1 × 10−2 (100)	unsteady
0.2857	28.7	M1	250	2869 (+832)	2.5×10^{-3}	yes	2.1×10^{-8} ($A = 5 \times 10^{-10}$) (100)	symmetric steady
0.2857	28.7	M1	250	878 (+7000)	5×10^{-3}	yes ($\mathrm{Re} = 42.9$)	2.1×10^{-8} ($A = 7 \times 10^{-12}$) (100)	symmetric steady
0.2857	42.9	M1	250	3897	5×10^{-3}	no	9.3×10^{-6} (100)	asymmetric steady
0.2857	42.9	M1	250	6000 (+1000)	5×10^{-3}	yes	9.3×10^{-6} ($A = 3 \times 10^{-7}$) (100)	asymmetric steady
0.2857	85.7	M1	250	3925 (+2000)	5×10^{-3}	yes	1.4×10^{-5} ($A = 1 \times 10^{-8}$) (100)	asymmetric steady
0.2857	114.3	M1	250	5342 (+2000)	5×10^{-3}	yes	1.0×10^{-5} ($A = 4 \times 10^{-9}$) (100)	asymmetric steady
0.2857	121.4	M1	250	7325 (+1000)	5×10^{-3}	yes	1.7×10^{-7} (100)	asymmetric steady
0.2857	128.6	M1	250	6800 (+1000)	5×10^{-3}	yes	5.0×10^{-6} ($A = 4 \times 10^{-5}$) (100)	asymmetric steady
0.2857	142.9	M1	250	5004 (+1000)	5×10^{-3}	yes	4.4×10^{-3} ($A = 4 \times 10^{-2}$) (100)	unsteady
0.3333	50	M1	250	1675	5×10^{-3}	no	2.2×10^{-8} ($A = 3 \times 10^{-8}$) (100)	symmetric steady
0.3333	50	M1	250	3877 (+1328)	5×10^{-3}	yes	2.2×10^{-8} (100)	symmetric steady
0.3333	40	M1	250	1602 (+3949)	5×10^{-3}	yes ($\mathrm{Re} = 60$)	2.3×10^{-8} ($A = 2 \times 10^{-8}$) (100)	symmetric steady
0.3333	50	M1	250	2377 (+3949)	5×10^{-3}	yes ($\mathrm{Re} = 60$)	7.1×10^{-7} ($A = 4 \times 10^{-4}$) (100)	asymmetric steady
0.3333	60	M1	250	2626 (+1323)	5×10^{-3}	yes	1.4×10^{-6} (100)	asymmetric steady
0.3333	60	M1	250	3676	5×10^{-3}	no	2.2×10^{-8} (100)	asymmetric steady
0.3333	66.7	M1	250	5930	5×10^{-3}	no	5.2×10^{-5} (100)	asymmetric steady
0.3333	100	M1	250	3344	5×10^{-3}	no	1.9×10^{-8} (100)	asymmetric steady
0.3333	133.3	M1	250	1252 (+1260)	5×10^{-3}	yes	3.0×10^{-6} (100)	asymmetric steady
0.3333	150	M1	250	2503 (+1856)	5×10^{-3}	yes	3.9×10^{-3} (100)	unsteady
0.3333	150	M1	250	4552	5×10^{-3}	no	6×10^{-3} (100)	unsteady
0.3333	166.7	M1	250	9557	5×10^{-3}	no	7.6×10^{-3} (100)	unsteady
0.3333	183.3	M1	250	3591	5×10^{-3}	no	1.6×10^{-2} (100)	unsteady

TABLE II. Simulation parameters, $m = 0.4348$–1, and $We = 10$.

m	Re_{inner}	Grid	L	T_{DNS} ($+T_{sfd}$)	ΔT	From steady?	Final residual (average time)	Final state
0.4348	54.3	M1	250	2505 (+1135)	5×10^{-3}	yes (Re = 76.0)	2.2×10^{-8} ($A = 3 \times 10^{-9}$) (100)	symmetric steady
0.4348	65.2	M1	250	1992	5×10^{-3}	no	2.2×10^{-8} (100)	symmetric steady
0.4348	65.2	M1	250	4000 (+8341)	5×10^{-3}	yes (Re = 76.1)	1.2×10^{-7} ($A = 4 \times 10^{-5}$) (100)	asymmetric steady
0.4348	76.1	M1	250	1740 (+6601)	5×10^{-3}	yes (Re = 97.8)	8.1×10^{-8} ($A = 3 \times 10^{-5}$) (100)	asymmetric steady
0.4348	87.0	M1	250	3519	5×10^{-3}	no	2.1×10^{-8} (100)	symmetric steady
0.4348	87.0	M1	250	4000 (+2001)	5×10^{-3}	yes	1.6×10^{-6} ($A = 1 \times 10^{-6}$) (100)	asymmetric steady
0.4348	97.8	M1	250	4000 (+2201)	5×10^{-3}	yes	2.1×10^{-8} (100)	asymmetric steady
0.4348	97.8	M1	250	5753	5×10^{-3}	no	1.2×10^{-5} (100)	asymmetric steady
0.4348	113.9	M1	250	3420	5×10^{-3}	no	2.0×10^{-8} (100)	asymmetric steady
0.4348	130.4	M1	250	4000 (+1052)	5×10^{-3}	yes	1.9×10^{-8} (100)	asymmetric steady
0.4348	152.2	M1	250	5855 (+2093)	5×10^{-3}	yes	1.8×10^{-8} (100)	asymmetric steady
0.4348	173.9	M1	250	8949 (+2090)	5×10^{-3}	yes	2.0×10^{-8} (100)	asymmetric steady
0.4348	195.7	M1	250	7873 (+3155)	5×10^{-3}	yes	1.3×10^{-4} (100)	unsteady
0.4348	239.1	M1	250	5282 (+3100)	5×10^{-3}	yes	1.6×10^{-2} (100)	unsteady
0.5	62.5	M1	250	2613 (+1200)	5×10^{-3}	yes (Re = 80)	2.1×10^{-8} (100)	symmetric steady
0.5	62.5	M1	250	1983	5×10^{-3}	no	2.2×10^{-8} (100)	symmetric steady
0.5	80	M1	250	2245 (+8000)	5×10^{-3}	yes (Re = 110)	1.0×10^{-6} (100)	asymmetric steady
0.5	95	M1	250	3737	5×10^{-3}	no	2.2×10^{-8} (100)	symmetric steady
0.5	95	M1	250	4000 (+2000)	5×10^{-3}	yes	2.1×10^{-8} (100)	asymmetric steady
0.5	110	M1	250	6000 (+2000)	5×10^{-3}	yes	1.4×10^{-6} ($A = 2 \times 10^{-6}$) (100)	asymmetric steady
0.5	110	M1	250	6000	5×10^{-3}	no	2.0×10^{-8} (100)	asymmetric steady
0.5	125	M1	250	6000 (+1906)	5×10^{-3}	yes	1.2×10^{-5} ($A = 6 \times 10^{-6}$) (100)	asymmetric steady
0.5	150	M1	250	2000 (+2000)	5×10^{-3}	yes	1.8×10^{-4} (100)	asymmetric steady
0.5	175	M1	250	7555 (+2000)	5×10^{-3}	yes	1.8×10^{-8} (100)	asymmetric steady
0.5	200	M1	250	7156 (+2000)	5×10^{-3}	yes	2.0×10^{-8} (100)	asymmetric steady
0.5	212.5	M1	250	9153 (+2000)	5×10^{-3}	yes	1.5×10^{-4} (100)	unsteady
0.5	225	M1	250	12102 (+2000)	5×10^{-3}	yes	1.3×10^{-4} (100)	unsteady
0.5	250	M1	250	8000	5×10^{-3}	no	3.0×10^{-4} (100)	unsteady
0.5	262.5	M1	250	5000	5×10^{-3}	no	4.1×10^{-4} (100)	unsteady
0.5	262.5	M1	250	1401 (+3180)	5×10^{-3}	yes	6.5×10^{-3} (100)	unsteady
0.5	275	M1	250	2651 (+4000)	5×10^{-3}	yes	2.2×10^{-2} (100)	unsteady
0.6667	83.3	M1	250	2000	5×10^{-3}	no	2.2×10^{-8} (100)	symmetric steady
0.6667	120	M1	250	2028 (+1205)	5×10^{-3}	yes (Re = 146.7)	1.4×10^{-7} ($A = 8 \times 10^{-5}$) (100)	asymmetric steady
0.6667	126.7	M1	250	1787	5×10^{-3}	no	2.1×10^{-8} (100)	symmetric steady
0.6667	146.7	M1	250	1630	5×10^{-3}	no	2.1×10^{-8} (100)	symmetric steady
0.6667	146.7	M1	250	2000 (+1168)	5×10^{-3}	yes	2.1×10^{-8} ($A = 9 \times 10^{-10}$) (100)	symmetric steady
0.6667	146.7	M1	250	4129 (+13035)	5×10^{-3}	yes (Re = 166.7)	1.1×10^{-6} ($A = 7e - 4$) (100)	asymmetric steady
0.6667	166.7	M1	250	12000 (+1035)	5×10^{-3}	yes	3.6×10^{-6} (100)	asymmetric steady
0.6667	200	M1	250	11950 (+2094)	5×10^{-3}	yes	8.9×10^{-6} ($A = 5 \times 10^{-7}$) (100)	asymmetric steady
0.6667	216.7	M1	250	5677 (+1058)	5×10^{-3}	yes	7.7×10^{-4} ($A = 3e - 4$) (100)	unsteady
0.6667	233.3	M1	250	5977 (+1011)	5×10^{-3}	yes	4.4×10^{-4} (100)	unsteady
0.6667	283.3	M1	250	3537 (+4315)	5×10^{-3}	yes	7.0×10^{-3} (100)	unsteady
0.6667	316.7	M1	250	3120 (+3180)	5×10^{-3}	yes	2.1×10^{-2} (100)	unsteady
0.7692	173.1	M1	250	2657 (+2000)	5×10^{-3}	yes (Re = 211.5)	2.0×10^{-8} ($A = 4 \times 10^{-7}$) (100)	symmetric steady
0.7692	192.3	M1	250	1601	5×10^{-3}	no	1.9×10^{-8} (100)	symmetric steady
0.7692	192.3	M1	250	2669 (+2000)	5×10^{-3}	yes (Re = 211.5)	1.9×10^{-8} ($A = 2 \times 10^{-6}$) (100)	symmetric steady
0.7692	211.5	M1	250	3934	5×10^{-3}	no	1.9×10^{-8} (100)	symmetric steady
0.7692	211.5	M1	250	4000 (+1162)	5×10^{-3}	yes	1.9×10^{-8} ($A = 7 \times 10^{-10}$) (100)	symmetric steady
0.7692	211.5	M1	250	(+)	5×10^{-3}	yes (Re = 230.8)	(100)	symmetric steady
0.7692	230.8	M1	250	4000 (+1009)	5×10^{-3}	yes	2.3×10^{-8} (100)	asymmetric steady
0.7692	250	M1	250	11618 (+1135)	5×10^{-3}	yes	6.8×10^{-4} (100)	unsteady
0.7692	269.2	M1	250	8000 (+3178)	5×10^{-3}	yes	2.6×10^{-4} (100)	unsteady

TABLE II. (*Continued*.)

m	$\mathrm{Re}_{\mathrm{inner}}$	Grid	L	T_{DNS} $(+T_{sfd})$	ΔT	From steady?	Final residual (average time)	Final state
0.7692	296.2	M1	250	6423 (+1078)	5×10^{-3}	yes	2.7×10^{-2} (100)	unsteady
0.7692	326.9	M1	250	5279 (+3171)	5×10^{-3}	yes	3.2×10^{-2} (100)	unsteady
0.9091	254.5	M1	250	6000 (+6591)	5×10^{-3}	yes	1×10^{-5} ($A = 3 \times 10^{-7}$) (100)	steady
0.9091	272.7	M1	250	6000 (+2906)	5×10^{-3}	yes	2.8×10^{-4} ($A = 1 \times 10^{-3}$) (100)	unsteady
1	230	M1	250			no		symmetric steady
1	245	M1	250	2000 (+)		yes	1×10^{-5} ($A = 5 \times 10^{-11}$)	symmetric steady
1	250	M1	250			no		unsteady
1	500	M1	250			no		unsteady

TABLE III. Simulation parameters, $m = 1.1$–10, and $\mathrm{We} = 10$.

m	$\mathrm{Re}_{\mathrm{inner}}$	Grid	L	T_{DNS} $(+T_{sfd})$	ΔT	From steady?	Final residual (average time)	Final state
1.1	230	M1	250	1983 (+1250)	5×10^{-3}	yes	3.4×10^{-8} ($A = 1.1 \times 10^{-10}$) (100)	steady
1.1	250	M1	250	2000 (+4059)	5×10^{-3}	yes	1.9×10^{-8} ($A = 1.2 \times 10^{-11}$) (100)	steady
1.1	270	M1	250	3174 (+4308)	5×10^{-3}	yes	4×10^{-3} ($A = 1.4 \times 10^{-2}$) (100)	unsteady
1.5152	150	M1	250	1257 (+1932)	5×10^{-3}	yes	2.2×10^{-8} (100)	symmetric steady
1.5152	225	M1	250	2606 (+2177)	5×10^{-3}	yes	2.0×10^{-8} (100)	symmetric steady
1.5152	275	M1	250	5128 (+1156)	5×10^{-3}	yes	1.1×10^{-6} ($A = 1 \times 10^{-7}$) (100)	symmetric steady
1.5152	310	M1	250	4423 (+1230)	5×10^{-3}	yes	3.5×10^{-6} ($A = 4 \times 10^{-7}$) (100)	symmetric steady
1.5152	350	M1	250	5359 (+1207)	5×10^{-3}	yes	4.6×10^{-4} ($A = 7 \times 10^{-4}$) (100)	unsteady
2	90	M1	250	1295 (+2000)	5×10^{-3}	yes	2.2×10^{-8} (100)	symmetric steady
2	120	M1	250	2611 (+2042)	5×10^{-3}	yes	2.2×10^{-8} (100)	symmetric steady
2	150	M1	250	1286 (+1167)	5×10^{-3}	yes	2.2×10^{-8} (100)	symmetric steady
2	200	M1	250	3785 (+2248)	5×10^{-3}	yes	4.9×10^{-6} ($A = 9 \times 10^{-8}$) (100)	symmetric steady
2	250	M1	250	4521 (+1182)	5×10^{-3}	yes	2.5×10^{-6} ($A = 4 \times 10^{-7}$) (100)	symmetric steady
2	300	M1	250	4973 (+1113)	5×10^{-3}	yes	1.3×10^{-2} ($A = 2 \times 10^{-3}$) (100)	unsteady
2	350	M1	250	1589 (+1086)	5×10^{-3}	yes	1.9×10^{-2} ($A = 3 \times 10^{-2}$) (100)	unsteady
3	200	M1	250	4790	5×10^{-3}	no	1.6×10^{-6} (100)	symmetric steady
3	200	M1	250	3949 (+1315)	5×10^{-3}	yes	4.6×10^{-7} ($A = 2 \times 10^{-6}$) (100)	symmetric steady
3	225	M1	250	4646 (+1943)	5×10^{-3}	yes	1.1×10^{-4} ($A = 1 \times 10^{-4}$) (100)	unsteady
3	250	M1	250	1705	5×10^{-3}	no	1.2×10^{-2} (100)	unsteady
3	300	M1	250	2442	5×10^{-3}	no	2.1×10^{-2} (100)	unsteady
3	400	M1	250	721	5×10^{-3}	no	2.5×10^{-2} (100)	unsteady
3	500	M1	250	787	5×10^{-3}	no	3.3×10^{-2} (100)	unsteady
3	600	M1	250	757	5×10^{-3}	no	4.5×10^{-2} (100)	unsteady
3	700	M1	250	775	5×10^{-3}	no	5.0×10^{-2} (100)	unsteady
5	50	M1	250	795 (+689)	5×10^{-3}	yes	5.7×10^{-7} ($A = 2 \times 10^{-6}$) (100)	symmetric steady
5	100	M1	250	2095 (+1110)	1×10^{-3}	yes	5.8×10^{-6} ($A = 3 \times 10-4$) (100)	symmetric steady
5	200	M1	250	1463 (+442)	$1 \times 10-3$	yes	1.5×10^{-3} ($A = 2 \times 10-2$) (100)	unsteady
5	200	M1	250	1148	1×10^{-3}	no	1.8×10^{-3} (100)	unsteady
5	300	M1	250	3178	5×10^{-3}	no	2.9×10^{-2} (100)	unsteady
5	500	M1	250	786	5×10^{-3}	no	5.2×10^{-2} (100)	unsteady
5	600	M1	250	799	5×10^{-3}	no	7.3×10^{-2} (100)	unsteady
5	700	M1	250	728	5×10^{-3}	no	9.4×10^{-2} (100)	unsteady
5	800	M1	250	803	5×10^{-3}	no	1.1×10^{-1} (100)	unsteady
5	900	M1	250	783	5×10^{-3}	no	1.1×10^{-1} (100)	unsteady
10	75	M1	250	1464	5×10^{-3}	no	2.2×10^{-2} (100)	unsteady
10	150	M1	250	1077 (+800)	5×10^{-3}	yes	3.6×10^{-2} (100)	unsteady
10	250	M1	250	1111 (+800)	5×10^{-3}	yes	5.2×10^{-2} (100)	unsteady
10	300	M1	250	1098 (+793)	5×10^{-3}	yes	1.7×10^{-1} (100)	unsteady

TABLE IV. Simulation parameters and We = 2.

m	$\mathrm{Re}_{\mathrm{inner}}$	Grid	L	T_{DNS} $(+T_{\mathrm{prev}})$	ΔT	Initial condition?	Final residual (average time)	Final state
0.2	20	M1	250	634 (+1014)	2.5×10^{-3}	yes (We = 10, Re = 30, asymmetric)	6.6×10^{-5} ($A = 4 \times 10^{-5}$) (100)	steady
0.2	30	M1	250	1657 (+1014)	2.5×10^{-3}	yes (We = 10, asymmetric)	2.8×10^{-3} ($A = 3 \times 10^{-3}$) (100)	unsteady
0.5	45	M1	250	1982 (+2613)	5×10^{-3}	yes (We = 10, Re = 62.5, symmetric)	2.3×10^{-8} ($A = 9 \times 10^{-12}$) (100)	symmetric steady
0.5	62.5	M1	250	4362 (+6000)	5×10^{-3}	yes (We = 10, Re = 110, symmetric)	5.9×10^{-4} (100)	unsteady
0.5	80	M1	250	3237 (+2245)	5×10^{-3}	yes (We = 10, asymmetric)	3.1×10^{-3} (100)	unsteady
0.5	95	M1	250	3497 (+4000)	5×10^{-3}	yes (We = 10, symmetric)	3.6×10^{-3} (100)	unsteady
2	250	M1	250	2428 (+4521)	5×10^{-3}	yes (We = 10, symmetric)	5.6×10^{-5} (100)	symmetric steady
2	300	M1	250	3877 (+4973)	5×10^{-3}	yes (We = 10, symmetric)	1.9×10^{-8} (100)	symmetric steady
2	350	M1	250	3279 (+1589)	5×10^{-3}	yes (We = 10, unsteady)	9×10^{-7} (100)	symmetric steady
2	400	M1	250	4318 (+3279)	5×10^{-3}	yes (Re = 350)	1.7×10^{-6} (100)	symmetric steady
2	450	M1	250	1653 (+4973)	5×10^{-3}	yes (We = 10, unsteady)	7.2×10^{-5} (100)	symmetric steady
10	250	M1	250	618 (+4000)	1×10^{-3}	yes (We = 10, unsteady)	8.7×10^{-4} ($A = 6 \times 10^{-5}$) (100)	steady
10	300	M1	250	693 (+4000)	1×10^{-3}	yes (We = 10, unsteady)	2.0×10^{-2} ($A = 9 \times 10^{-5}$) (100)	unsteady (by inspection)

TABLE V. Simulation parameters and We = 5.

m	$\mathrm{Re}_{\mathrm{inner}}$	Grid	L	T_{DNS} $(+T_{\mathrm{prev}})$	ΔT	Initial condition?	Final residual (average time)	Final state
0.2	20	M1	250	2697 (+1159)	1×10^{-3}	yes (Re = 30)	5.0×10^{-5} ($A = 4 \times 10^{-10}$) (100)	symmetric steady
0.2	30	M1	250	1159 (+3653)	2.5×10^{-3}	yes (We = 10)	2.7×10^{-8} ($A = 3 \times 10^{-8}$) (100)	asymmetric steady
0.2	80	M1	250	1888 (+1492)	2.5×10^{-3}	yes	9.6×10^{-3} ($A = 2 \times 10^{-1}$) (100)	unsteady
0.2	90	M1	250	1700 (+925)	2.5×10^{-3}	yes	1.1×10^{-2} ($A = 3 \times 10^{-1}$) (100)	unsteady
0.5	50	M1	250	3160 (+2050)	2.5×10^{-3}	yes (Re = 160)	4.3×10^{-5} (100)	steady
0.5	80	M1	250	2050 (+2245)	2.5×10^{-3}	yes (We = 10)	2.7×10^{-3} (100)	unsteady
10	150	M1	250	1059 (+768)	1×10^{-3}	yes	1.2×10^{-5} ($A = 1 \times 10^{-11}$) (100)	symmetric steady
10	300	M1	250	1051 (+1098)	1×10^{-3}	yes	1.5×10^{-1} ($A = 7 \times 10^{-5}$) (100)	unsteady

TABLE VI. Simulation parameters and We = 20.

m	$\mathrm{Re}_{\mathrm{inner}}$	Grid	L	T_{DNS} $(+T_{\mathrm{prev}})$	ΔT	Initial condition?	Final residual (average time)	Final state
0.2	20	M1	250	356 (+1256)	1×10^{-3}	yes (Re = 30)	3×10^{-6} ($A = 1 \times 10^{-9}$) (100)	symmetric steady
0.2	30	M1	250	1256 (+3653)	2.5×10^{-3}	yes (We = 10)	1.9×10^{-8} ($A = 4 \times 10^{-9}$) (100)	asymmetric steady
0.2	80	M1	250	5133 (+1460)	2.5×10^{-3}	yes	1.4×10^{-4} ($A = 4 \times 10^{-8}$) (100)	asymmetric steady
0.2	90	M1	250	3204 (+1219)	2.5×10^{-3}	yes	1.8×10^{-3} ($A = 1 \times 10^{-3}$) (100)	unsteady
2	300	M1	250	3883 (+4973)	5×10^{-3}	yes (We = 10, unsteady)	5.2×10^{-6} ($A = 5 \times 10^{-9}$) (100)	symmetric steady
2	250	M1	250	2193 (+4973)	5×10^{-3}	yes (We = 10, steady)	6.3×10^{-7} (100)	symmetric steady

TABLE VII. Simulation parameters and We = ∞.

m	$\mathrm{Re}_{\mathrm{inner}}$	Grid	L	T_{DNS} $(+T_{\mathrm{prev}})$	ΔT	Initial condition?	Final residual (average time)	Final state
0.5	200	M1	250	1457 (+3781)	5×10^{-3}	yes (We = 10, unsteady)	6.0×10^{-3} ($A = 3 \times 10^{-7}$) (100)	unsteady (by inspection)
0.5	250	M1	250	2140 (+4973)	5×10^{-3}	yes (We = 10, unsteady)	6.7×10^{-3} ($A = 7 \times 10^{-7}$) (100)	unsteady (by inspection)
0.5	300	M1	250	1467 (+4973)	5×10^{-3}	yes (We = 10, unsteady)	7.5×10^{-3} ($A = 7 \times 10^{-7}$) (100)	unsteady (by inspection)

[1] P. A. M. Boomkamp and R. H. M. Miesen, Classification of instabilities in parallel two-phase flow, Int. J. Multiphase Flow **22**, 67 (1996).
[2] P. Yecko, S. Zaleski, and J.-M. Fullana, Viscous modes in two-phase mixing layers, Phys. Fluids **14**, 4115 (2002).
[3] C.-S. Yih, Instability due to viscosity stratification, J. Fluid Mech. **27**, 337 (1967).
[4] S. G. Yiantsios and B. G. Higgins, Linear stability of plane poiseuille flow of two superposed fluids, Phys. Fluids **31**, 3225 (1988).
[5] A. P. Hooper and W. G. C. Boyd, Shear-flow instability at the interface between two viscous fluids, J. Fluid Mech. **128**, 507 (1983).
[6] E. J. Hinch, A note on the mechanism of the instability at the interface between two shearing fluids, J. Fluid Mech. **144**, 463 (1984).
[7] S. J. Rees and M. P. Juniper, The effect of surface tension on the stability of unconfined and confined planar jets and wakes, J. Fluid Mech. **633**, 71 (2009).
[8] O. Tammisola, F. Lundell, and L. D. Söderberg, Effect of surface tension on global modes of confined wake flows, Phys. Fluids **23**, 014108 (2011).
[9] O. Tammisola, F. Lundell, and L. D. Söderberg, Surface tension-induced global instability of jets and wakes, J. Fluid Mech. **713**, 632 (2012).
[10] L. Biancofiore, F. Gallaire, and E. Heifetz, Interaction between counterpropagating Rossby waves and capillary waves in planar shear flows, Phys. Fluids **27**, 044104 (2015).
[11] L. Biancofiore, F. Gallaire, P. Laure, and E. Hachem, Direct numerical simulations of two-phase immiscible wakes, Fluid Dyn. Res. **46**, 041409 (2014).
[12] L. Ó. Náraigh, I. Bethune, and P. Valluri, TPLS, https://sourceforge.net/projects/tpls/ (2016).
[13] L. Ó. Náraigh, P. Valluri, D. M. Scott, I. Bethune, and P. D. M. Spelt, Linear instability, nonlinear instability and ligament dynamics in three-dimensional laminar two-layer liquid-liquid flows, J. Fluid Mech. **750**, 464 (2014).
[14] O. Tammisola, F. Lundell, P. Schlatter, A. Wehrfritz, and L. D. Söderberg, Global linear and nonlinear stability of viscous confined plane wakes with co-flow, J. Fluid Mech. **675**, 397 (2011).
[15] M. Sussman and E. Fatemi, An efficient, interface-preserving level set redistancing algorithm and its application to interfacial incompressible fluid flow, SIAM J. Sci. Comput. **20**, 1165 (1999).
[16] X. I. A. Yang and R. Mittal, Acceleration of the Jacobi iterative method by factors exceeding 100 using scheduled relaxation, J. Comput. Phys. **274**, 695 (2014).
[17] R. R. Nourgaliev and T. G. Theofanos, High-fidelity interface tracking in compressible flows: Unlimited anchored adaptive level set, J. Comput. Phys. **224**, 836 (2007).
[18] M. Juniper, O. Tammisola, and F. Lundell, The local and global stability of confined planar wakes at intermediate Reynolds number, J. Fluid Mech. **686**, 218 (2011).
[19] E. Åkervik, L. Brandt, D. S. Henningson, J. Hoepffner, O. Marxen, and P. Schlatter, Steady solutions of Navier-Stokes equations by selective frequency damping, Phys. Fluids **18**, 068102 (2006).
[20] L. Biancofiore, F. Gallaire, and R. Pasquetti, Influence of confinement on a two-dimensional wake, J. Fluid Mech. **688**, 297 (2011).
[21] O. Marquet, M. Lombardi, J. Chomaz, D. Sipp, and L. Jacquin, Direct and adjoint global modes of a recirculation bubble: Lift-up and convective non-normalities, J. Fluid Mech. **622**, 1 (2009).
[22] J. Samuelsson, O. Tammisola, and M. P. Juniper, Breaking axi-symmetry in stenotic flow decreases the critical transition Reynolds number, Phys. Fluids **27**, 104103 (2015).
[23] I. Lashgari, O. Tammisola, V. Citro, L. Brandt, and M. P. Juniper, The planar X-junction flow: Stability and control, J. Fluid Mech. **753**, 1 (2014).